

Constraining the Form of the Galactic Halo With Deep Star Counts

by

David Saul Davis

B.Sc.(Physics), McGill University, 2002

A THESIS SUBMITTED IN PARTIAL FULFILMENT OF
THE REQUIREMENTS FOR THE DEGREE OF

MASTER OF SCIENCE

in

The Faculty of Graduate Studies

(Department of Physics and Astronomy)

We accept this thesis as conforming
to the required standard

THE UNIVERSITY OF BRITISH COLUMBIA

October 2004

© David Saul Davis, 2004



Library Authorization

In presenting this thesis in partial fulfillment of the requirements for an advanced degree at the University of British Columbia, I agree that the Library shall make it freely available for reference and study. I further agree that permission for extensive copying of this thesis for scholarly purposes may be granted by the head of my department or by his or her representatives. It is understood that copying or publication of this thesis for financial gain shall not be allowed without my written permission.

DAVID SAUL DAVIS

Name of Author (please print)

08/10/2004

Date (dd/mm/yyyy)

Title of Thesis: CONSTRAINING THE FORM OF THE MILKY WAY HALO
WITH DEEP STAR COUNTS

Degree: M.Sc.

Year: 2004

Department of PHYSICS & ASTRONOMY

The University of British Columbia
Vancouver, BC Canada

Abstract

The Canada-France-Hawaii Telescope Legacy Survey – Deep (CFHTLS-Deep) represents a truly unique data set in terms of angular size and depth. Although the survey is only $\sim 40\%$ complete, it is already complete to a magnitude of 25 in u^*, g', r', i' , and z' . We use this data for an ambitious star-count project. By comparing the observed colour-magnitude diagrams (CMDs) with simulated CMDs, one can place many constraints on the form of the Galaxy. This thesis represent the first stage of this project – the study of the stellar halo of the Galaxy. We find the half-light radius of the de Vaucouleurs profile to be slightly higher than the literature value. We find the slope of the initial-mass function of stars with masses between $0.4M_{\odot} < M < 0.8M_{\odot}$ is slightly lower than Salpeter. We find that the halo is oblate with a ratio of minor axis to major axis of ~ 0.9 . Finally, we find that the best value of the stellar binary fraction is 0.35. The other elements of the CFHTLS (CFHTLS-Wide and CFHTLS-Very Wide) provide an immense number of observations that can be compared with theoretical models. There is plenty of data with which to constrain the form of the other components of the Galaxy – the thick and thin disks. This study, along with the subsequent studies, will give us the most detailed picture of the stars in our home Galaxy ever.

Contents

Abstract	ii
Contents	iii
List of Tables	v
List of Figures	vi
1 Introduction	1
1.1 The History of Star Counting	1
1.2 Thesis Goals	4
1.3 Present Status	5
1.4 Layout	7
2 Data	9
2.1 CFHT Open Star Cluster Survey	9
2.1.1 Data Reduction	10
2.1.2 Calibration	11
2.1.3 Combination of deep and shallow exposures	13
2.2 CFHT Legacy Survey	14
2.2.1 Reduction	15
2.2.2 Star-galaxy separation	18
3 The models	33
3.1 Monte Carlo Simulations	34

3.2	Probability Map	37
4	Data – Model comparison	43
4.1	Statistics	43
4.1.1	Gaussian Likelihood Ratio	43
4.1.2	Poisson Likelihood Ratio	44
4.1.3	Bayesian Inference	45
4.2	Parameter Search and Error Estimation	46
4.2.1	Searching Parameter Space	46
4.2.2	Error Estimation	50
5	Constraints on Parameters	51
5.1	Initial Mass Function	51
5.2	Physical size	59
5.3	Axial ratio	59
5.4	Binary fraction	62
6	Conclusions and Discussion	65
6.1	Conclusions	65
6.2	Discussion	66
6.3	Future Work	66
	Bibliography	68

List of Tables

2.1	Coordinates of the centers of the CFHTLS-Deep fields	15
-----	--	----

List of Figures

2.1	The locations of the CFHTLS-Deep fields	16
2.2	CMD of D4	20
2.3	Fan's colour-magnitude space selection	21
2.4	Half-light radius vs. magnitude	23
2.5	CMD with HLR cut	24
2.6	Fan colour-colour space selection	25
2.7	Colour-Colour diagram	26
2.8	CMD with colour-colour selection	27
2.9	Colour-colour selection	28
2.10	CMD with colour-colour selection	29
2.11	Stellarity vs. magnitude	30
2.12	CMD of D1, D2, D3 & D4	32
3.1	Schematic of simulations	35
3.2	Monte Carlo CMD	38
3.3	Probability maps	41
3.4	Number densities vs. distance modulus	42
5.1	Contour plot – D1	52
5.2	Contour plot – D2	53
5.3	Contour plot – D3	54
5.4	Contour plot – D4	55
5.5	IMF vs. BF	57

5.6	IMF vs. axial ratio	58
5.7	HLR vs. binary fraction	60
5.8	HLR vs. AR	61
5.9	Binary fraction vs. AR	63

Acknowledgments

I would like to thank my supervisor, Dr. Harvey Richer. This thesis would not have been possible without his ideas, encouragement and support. I am indebted to him for giving me the opportunity to conduct my research in many places around the world, and to collaborate with experts in the field. I would like to thank Jasper Wall, who led me down the correct path in terms of statistical analysis. I would like to thank Michele Cignoni. His three years of hard work gave us a framework within which to conduct the project. Furthermore, his stellar evolutionary tracks were indispensable. I would like to thank Giuseppe Bono for being such a gracious and attentive host for the duration of my stay in Monte Porzio. I would like to thank Jason Kalirai for being so patient while explaining the basic concepts of stellar photometry. I would like to thank Anna Sajina for helping me conceptualize Markov Chain Monte Carlos. I would like to thank Robert Ferdman, Jason Rowe, and Mark Huber for dealing with my endless barrage of Fortran, Linux, and awk questions. Finally, I'd like to give a shout out to Céline for making sure that I ate and slept everyday for the duration of the project.

Chapter 1

Introduction

1.1 The History of Star Counting

Galaxy formation is one of the most actively pursued fields in modern astrophysics. The most direct approach is to detect high redshift galaxies as they are forming. This approach has proved to be successful at answering a large range of questions. However, there is an alternate approach. The galaxies in the Local Group can be studied in detail unimaginable for high redshift galaxies. The absolute magnitudes, metallicities and velocities of individual stars may be measured. If the record of galaxy formation is imprinted in some observable of these stars, we have an alternate and independent approach with which to answer fundamental questions regarding galaxy formation. Indeed the manner in which a particular galaxy formed is imprinted in its stars. The stellar age, metallicity, and distribution in phase space all give clues to the way in which a Galaxy formed. Because of our proximity to stars in the Milky Way, the Galaxy is one of the best places to conduct a study of this nature. Only in the Milky Way are large numbers of low mass stars easily resolvable. If one can reconstruct a detailed model of the Galaxy, then it becomes possible to perform ‘stellar archeology’, and gain insight into processes that occurred when the Universe was a fraction of its current age. In this thesis I conduct a study of the Milky Way halo via comparison of observations with predictive star-count models.

In the early 1600s Galileo resolved the band of light known as the Milky Way into separate stars. This fundamental result paved the way for following generations of scientists to understand the nature of our home Galaxy. In the mid-1700s, Emanuel Kant and Thomas Wright proposed that the circular nature of the Milky Way could be ex-

plained if the Galaxy was a vast stellar disk and our solar system was merely a small component[5]. This postulate represented the first recognition that we live in a galaxy that was not spherical. Counting stars was one of the first quantitative studies undertaken by astronomers, yet it remains a fruitful endeavor to this day.

In the 1780s William Herschel produced the first map of the Milky Way. His map was based on counting the number of stars in 683 separate regions of the sky. By today's standard, his understanding of stars was extremely crude. In order to interpret his results he simplified his analysis by assuming that the intrinsic luminosity of all stars was equal, the stellar density throughout the Galaxy was constant, there was no obscuring medium between the stars, and the end of the stellar distribution was visible. From his data, Herschel concluded that the sun was at the centre of a distribution with a vertical extent one fifth that of its horizontal extent[5].

Star-count models took a leap forward with the work of Jacobus Kapteyn. His work, during the early 20th Century, confirmed Herschel's conclusions, albeit in a much more quantitative manner. Kapteyn was able to associate a physical distance and scale lengths with his model. The Kapteyn "Universe" consisted of a flattened spheroidal system of stars. The stellar density dropped steadily, and decreased to 50% of its peak value 800 pc and 150 pc from the center along the major axis and minor axis respectively, and to 1% by 8500 pc and 1700 pc along the same axes. He concluded that the Sun lay at a distance of 650 parsecs from the centre, 38 pc above the Galactic mid-plane[5].

Star-count models became very popular after Kapteyn. In the 1920's and 30's these models were used by the likes of Bok[9], Basinski[2], Seares[32], Van Rhijn [33], and Oort[23] in a effort to determine the geometrical form of the Galaxy in terms of its stars and dust. These efforts concentrated on directly inverting the equations of stellar statistics, and met with limited success for several reasons. First, dust is distributed in a stochastic manner throughout the disk of the Galaxy. Although there are general trends to the distribution, such as decreasing levels of dust at higher Galactic latitudes, there exist patches of dust that buck the general trend. Secondly, the relatively shallow limiting magnitude of the data then available led to a relatively small number of stars

by today's standards. The inversion of the integral equation for the projected number of stars on the sky is an unstable mathematical function, and produces unreliable results for small numbers of stars. For these reasons, interest in star-count models of the Galaxy waned during the middle of the 20th century.

Star-count models went through a renaissance in the 1980's with the publication of the Bahcall & Soneira's model[1]. Bahcall credited the renewed interest in star counts to three factors: 'the use of automatic measuring devices, a change of theoretical tactics, and these developments of a detailed model that can be used with modern computers.' [1] All three of the developments occurred, more or less concurrently in the early 1980's, and each is essential to the modern field of star counting. The use of automatic measuring devices for photographic plates, and the subsequent development of CCDs, led to a revolution in terms of the number, and accuracy, of stellar photometric measurements available. The change in theoretical tactics was to abandon the attempt to map the dust distribution in the Galaxy. Rather, the focus was placed on patches of the sky that had very low extinction. Finally, the geometrical form of the Galaxy was assumed to be that of other galaxies of similar Hubble type. These so called 'copy cat' models do not attempt to yield a unique solution to the form of the Galaxy, but rather attempt to restrict the possible parameter space that accurately describes the Galactic form by iteratively comparing models with observations.

With the advent of large mosaiced charge coupled devices (CCDs), and powerful computers, using the technique of star-counts to place meaningful constraints on the form on the Milky Way has become feasible. These developments open a door to exploring the Milky Way in a manner that was never before possible. In 1996 Ried et al. conducted a major study of the Milky Way halo attempting to determine the luminosity function of the halo at very small masses ($0.5M_{\odot}$). Taking advantage of the extremely good seeing ($0.5''$) during his observing run, he was able to distinguish stars from galaxies to a magnitude of $R = 24.5$. However, he was limited in colour to $(R-I) < 1$ by confusion with thin disk M-dwarfs. Unfortunately, the lowest mass main-sequence stars have redder $(V-I)$ colours than $(V-I)=1$. He was unable to put constraints on the luminosity function

at very low masses.[26]

The advent of the Sloan Digital Sky Survey (SDSS) led to an increased interest in star-count models. In 1999 Fan conducted an important theoretical study predicting where different contaminating populations (eg. QSOs) would lie in colour-colour space[8]. Although the SDSS had extremely large areal coverage (~ 1000 square degrees), the limiting magnitude of the study was relatively bright ($g' \sim 22$). A study by Chen et al.[6] attempted to determine the degree of flattening of the halo, and to fit the density of the halo to a power law. Although the combination of the two were highly degenerate the best fitting combination was determined to be a very flattened halo ($c/a \sim 0.55$) and a relatively flat power law index (2.5 ± 0.3)[6].

There have also been several attempts to constrain the star formation history of both the disk of the Galaxy, and local dwarf galaxies. Some examples of these include papers by Vallenari et al.[37], Robin et al.[28], and Dolphin[7]. Although the paper by Dolphin was concerning dwarf spheroidal galaxies, it was particularly useful for this project because of the rigorous statistical analysis it contained.

Recently there have been several more studies of the Galactic Halo. The most recent of these is a study by Lemon et al. [21]. This study was based on SDSS and the Millennium Galaxy catalogue, and again found a flattened halo ($c/a = 0.56$). These projects are always plagued by similar problems. First, there is only a small colour-magnitude space that is dominated by the Galactic halo. Second, the derived parameters are often quite co-variant with one another. There has been no study that attempts to constrain more than two parameters simultaneously. This thesis will focus on the author's recent efforts toward this end.

1.2 Thesis Goals

The goal of this thesis is to be able to put tight constraints on all parameters necessary to describe the form of the Galactic Halo. It is important to realize that the method of predictive star-count models can never yield a unique solution due to the fact that a

small perturbation may be added to any well fitting model without significantly changing the value of the fit. Recognizing this, in accordance with Occam's razor, one attempts to construct a model with the fewest number of parameters that can model all the essential observational features with an acceptable accuracy. Furthermore, one must ensure that none of the assumptions that are used in the model (i.e. geometrical form of the population) is not overly restrictive. As the data improve, the number of observable stars, and the limiting magnitude of those stars increase. With an increased number of stars, signal to noise is increased, and one may add more elements to the model. The correct number of elements to include in a model can be determined by experimenting with statistics such as the run test.

For the purposes of this thesis we restrict ourselves to the study of a Galactic Halo hypothesized to be well described by five parameters. These are a normalizing number density of halo stars, slope of the initial-mass function for stars with masses between $0.4M_{\odot}$ and $0.8M_{\odot}$, half-light radius of the halo, binary fraction, and ratio between the major and minor axes of the halo.

The potential of this study extends far beyond the scope of this thesis. The high density of stars in the disk allows for a more in depth study. The more complicated form of the disk requires a larger number of free parameters than a model of the halo. When attempting to model the Galactic disk a typical Megacam field will contain tens of thousands of stars, compared with several hundred halo stars. With numbers like these, one can imagine fitting a model that includes: scale length, scale height, star-formation history, metallicity gradients, binary fraction, the slope of the initial-mass function over several mass ranges, and the local stellar density of disk stars.

1.3 Present Status

A large portion of this project was made up of developing an approach with which to attack the problem. This approach had several components. The first of these was to discover the correct question to ask. The beginning of this project focused on the spiral

structure of the Galaxy. While this is a very interesting question, it is an extremely challenging one. The clumpy distribution of dust throughout the Galaxy makes it impossible to suppose an analytical model that can predict the true dust distribution. Without an independent measure of reddening as a function of distance from the sun, predictive star count models have a very small chance at success. It was realized that it would be far more fruitful to concentrate on fields with high Galactic latitude. This changed the focus of the study from attempting to constrain the spiral structure of Milky Way to a focus on the form of the Milky Way halo.

The second challenge was the choice of data. During the earlier phases of the project we attempted to use data from the Canada-France-Hawaii Telescope Open Star Cluster Survey (CFHT-OSCS). While there is certainly a large amount of information contained in these fields, they are not appropriate for a study of this scope. It was only realized relatively recently that the CFHT Legacy Survey (CFHTLS) is an ideal source of data for this project. This data has now been reduced. Furthermore, scripts have been developed which means that any further reductions can be performed quickly and easily.

When attempting to use predictive star-count models to constrain Galactic structure, it goes without saying that one must make predictions. These predictions typically take the form of ‘artificial data’. The third challenge was to determine the method to produce the artificial data, and indeed in what form it was most useful. It was first assumed that the most useful form of the simulated data would be the same for that the observed data was in – a photometry list. To create data in this form, the best technique is a Monte Carlo simulation. A Monte Carlo simulation code, MILKYWAYMC, was written by Michele Cignoni. Later, it was realized that it was more efficient to compare the observed photometry with probabilities directly. This necessitated the development of a code that was able to produce a map of probabilities in colour-magnitude space, MILKYWAYPM. Both these codes are now functioning, and promise to be very useful in future studies.

The fourth challenge was the determination of the technique used to compare the simulated and observed data. Several different methods were used. At first, Hess diagrams were employed to compare the quality of fits of different models. For this technique to

be useful, it must be used in a regime where points are distributed with Gaussian errors. This project is not in this regime. Comparing luminosity functions, and colour functions were also experimented with, but found to be difficult to interpret. Eventually, we came upon a useful statistic with which to determine maximum likelihoods in the Poisson regime, namely the Poisson likelihood ratio.

The fifth challenge was determining a manner in which to search a high-dimensional parameter space. We experimented with several different approaches from the simple grid search to more complicated Markov Chain Monte Carlos, gradient calculations, and simplex methods.

All the aforementioned challenges have been met, and we now possess a unique data set and a powerful algorithm with which to analyse it. Fields that are dominated by the halo of the Galaxy, taken from the CFHTLS-Deep, have been analysed. However, as the Legacy Survey will continue to accumulate images of the aforementioned fields, the photometry will continue to improve. As the analysis of the fields has been automated, it takes little effort to re-analyse the fields as more data become available. At the moment we are limited not by the depth of the photometry, but by our inability to distinguish stars from galaxies at faint magnitudes. If this problem can be overcome we will be able to take full advantage of the data we have in hand. If indeed we can access the data fainter than $g' = 25$ we have a marvelous opportunity to study the lowest mass stars in the halo – stars that are generally inaccessible to other star count studies.

1.4 Layout

This thesis will follow the following form:

Chapter 2 will be devoted to discussing the particular data that has been, and will be used for this project. There are two distinct sources of data used in this project, and both will be discussed in turn. The first source of data were from the CFHTLS-Deep. These data were the primary source of information in the analysis of the

Galactic Halo. The second source of data is the CFHT Open Star-Cluster Survey (CFHT-OSCS). These data will be used in further studies of the Galactic disk.

Chapter 3 will discuss the details of the model used to simulate the Galaxy. The model, coauthored by myself and Michele Cignoni from the University of Pisa, was developed in the spirit of Bachall & Soneira. The Galaxy is modeled as consisting of three independent components: the halo, the thick disk, and the thin disk. Whereas most preceding models used an empirically determined luminosity function to predict stellar counts, these models use a theoretical initial-mass function (IMF) and stellar evolutionary tracks to predict stellar counts. This yields the enviable ability to place observational constraints on the stellar IMF, and star-formation history of the Galaxy.

Chapter 4 will discuss the various statistics used to compare the observed CMDs with the simulated one. This was a critical aspect of the project. Furthermore, it will discuss the methods used to determine the best fitting parameters. The methods discussed will highlight the advantages and disadvantages of various parameter search techniques in multi-dimensional parameter spaces – specifically the downhill simplex method, the Markov Chain Monte Carlo, and the grid search. Finally, we will discuss the method for determining the error on the fitted parameters.

Chapter 5 will discuss the results we obtained from our analysis. We present results for the halo; these results demonstrate the power of the technique.

Chapter 6 will conclude and discuss the direction of future work on this project.

Chapter 2

Data

The data used for this study came primarily from two sources: The Canada-France-Hawaii Telescope Open Star Cluster Survey (CFHT-OSCS) and the Canada-France-Hawaii Telescope Legacy Survey (CFHT-LS). The two data sets required different levels of processing and therefore will be discussed in the separate sections.

2.1 CFHT Open Star Cluster Survey

The Canada-France-Hawaii Telescope Open Star Cluster Survey was an ambitious study originally intended to obtain deep ($V \sim 24.5$) multi-colour photometry of 19 open star clusters in the disk of the Milky Way. The CFHT-OSCS is a data set of unprecedented depth and area compared with previous open star cluster studies. The study had the ambitious goals of the comparison of observational results and theoretical models, the study of star-cluster dynamics, and the determination of the distance to and age of the clusters. To date five papers have been published directly on the study, and many collaborations have used the data in some other way.

The data for the 19 open clusters was taken during a three-night observing run with the Canada-France-Hawaii Telescope (CFHT) from October 15 to October 18, 1999. The images were taken with CFH-12K, a high-resolution, wide-field mosaic camera, mounted at the f/4 prime focus of CFHT. The camera is made up of twelve 2048×4096 pixel CCDs with an angular size of 0.206 arcseconds/pixel. The wide field of the camera was necessary for imaging open clusters with a large angular extent. Fortunately, the clusters often only filled the inner four chips of the camera, leaving 2/3 of the camera available to obtain uncontaminated images of the background populations.

Images of the clusters were taken in three filters: Johnson B,V, and R. The R images were shallow, and were used only to get an estimate of the reddening to the cluster. The choice of B and V filters rendered the survey rather sensitive to dust extinction – not an ideal choice for this study. However, the primary science goals of the project was the study of white dwarfs, and it was this consideration that drove the filter selection. Furthermore, it was this goal that determined the limiting magnitudes of the various fields. In most cases the observations had a limiting magnitude of $V \sim 24.5$ at a colour of $(B - V) = 0$, but unfortunately significantly brighter at redder colours. For the majority of the clusters, it was determined that a single 300s second exposure was sufficient to meet the goals. For several of the clusters, deeper images were obtained by stacking several 300s exposures. It is these fields that are of the most use for this spin off study.

Because of the very low Galactic latitude of the majority of these fields, the star counts are dominated by the Galactic thin disk. This thesis will be concentrating on the Galactic halo, and therefore this data will not be used directly in this thesis. However, as this project continues, and the analysis expands to include the Galactic disk, this data will become extremely useful. Furthermore, many of the principles involved in this reduction were also used to reduce the CFHTLS data, and hence were necessary for the ultimate completion of the project.

2.1.1 Data Reduction

The first stage of the reduction involves the preprocessing. The preprocessing of this data were performed by Jason Kalirai as part of his M.Sc. thesis. The preprocessing can be divided into several steps:

1. Bias frames (exposure time = 0 s) and dark current frames are taken, and subtracted from the science frame. This accounts for the non-zero readout from a CCD even if the CCD is not exposed to any light.
2. After the images are de-biased, the data is flat-fielded. This involves taking images of an even background such as the twilight sky, or a screen inside the dome. The

differing responses of the individual pixels is calibrated in this way.

3. These corrections are applied using the FITS Large Images Processing Software (FLIPS). Furthermore, one may normalize the sky background to the chip with the highest sky value (lowest gain), CCD4. This step provides a scaled data set with a smooth background on all chips, and consequently the zero points for all the chips will be nearly equal. For the CFHT-OSCS the flat field was good to better than 1% in all filters.
4. In order to reach the faintest magnitudes, multiple deep exposures were taken of several of the clusters. These multiple deep exposures were stacked and averaged using FLIPS.
5. The photometry was performed using Emanuel Bertin's SExtractor and PSFex software packages. These are highly automated, very fast programs that quickly produce accurate photometry for moderately crowded fields. These programs are ideal for extracting photometry for the huge numbers objects present in the modern astronomical surveys.

2.1.2 Calibration

Calibration is a difficult but critical step in the creation of a useful photometric catalog. In order to convert the instrumental magnitudes to real magnitudes we use the following equations:

$$v_{instr} = V + \alpha_v X + \beta_v (B - V) + Z_v \quad (2.1)$$

$$b_{instr} = V + \alpha_b X + \beta_b (B - V) + Z_b \quad (2.2)$$

In the above equations v_{instr} and b_{instr} are instrumental magnitudes given by PSFex, α is the coefficient of the air-mass term X , β is the coefficient of the colour correction term $(B - V)$, and Z is the zero-point shift. A total of 23 calibration frames of different exposure times, air-masses, and filters were used to calculate the various coefficients, and solve for the calibrated apparent magnitudes. There are subtle systematic differences

between each chip, so individual calibrations are required for every chip, and further for every individual cluster. The value of β remains constant for all nights of observation. The vast majority of the difference between the different calibrations is accounted for by the zero-point term, Z .

When one desires to compare their photometric measurements with another study, that may have used a slightly different set of broadband filters, it is of utmost importance that the magnitude systems used are consistent with one another. In 1983, Landolt published a catalogue of bright stars ($11.5 < V < 16.0$) around the celestial equator [15]. This allowed for people using slightly different filter sets to compare their photometric measurements directly. The magnitudes of the standard stars used by Landolt are based on non-linear transformations of the magnitudes and colours of the stars in several different filters. The final magnitudes derived for the stars are based on the total amount of flux emitted in a filter within a large aperture designed to ensure minimal light is lost. In contrast, PSFex fits the point spread functions of the stars such that signal-to-noise ratio is maximized. This means that some of the flux from the star is sacrificed in order to eliminate flux from the sky. In order to calibrate the data, total flux must be compared with total flux. Therefore, it is required that aperture photometry is used in conjunction with PSF photometry during the calibration phase.

To solve for the calibration coefficients one must find many unsaturated stars, with high signal to noise, that appear both in Landolt's catalogue[16][17] and the calibration images taken of the Landolt standard fields: SA-92 and SA-95. DAOPHOT was used to calculate the magnitudes of stars with various apertures, ranging from 8 – 20 pixels. From this data, a curve of growth was constructed. It was found that an aperture of 16 pixels, the measured magnitude was within 0.01 Mag (99% of the total flux) of its final value, and the flux from the sky was minimized. It was these magnitudes that were compared with the standard magnitudes taken from Landolt.

The calibration coefficients were calculated by using a least squares method, in which a large number of stars that satisfy the above criteria (i.e. high signal to noise, unsaturated, and appearing on both Landolt's catalogue and calibration images) are fit simultaneously

for all three coefficients in both the B and V filters. The specific algorithm was based on a method designed by Harris, Fitzgerald & Reed [11]. Unfortunately, not all chips contain enough stars that fit these criteria to obtain a low-sigma fit. Including fits that do not have an acceptable sigma do not aid with the analysis, and are therefore disregarded. In this case, only chips 02, 04, 07, and 08 gave results that had an acceptable sigma. However, these four independent calibrations were all very close to each other, making it reasonable to extend these results to the other chips. From this stage we take away the following coefficients: Z_v , Z_b , α_v , α_b , β_v , and β_b .

We then create on-frame science standards. The stars selected to be on-frame standards are bright, yet unsaturated. Using the following equations:

$$V = v_{PSF} - \beta_v(B - V) - Z'_v - 2.5 \log(t) \quad (2.3)$$

$$B = b_{PSF} - \beta_b(B - V) - Z'_b - 2.5 \log(t) \quad (2.4)$$

we determine Z'_v and Z'_b where Z'_v and Z'_b represent the final shifts from the instrumental magnitudes to the apparent magnitudes. We then solve equations 2.1 and 2.2 for the terms $V + \beta_v(B - V)$ and $B + \beta_b(B - V)$ which are then substituted back in equations 2.3 and 2.4 along with the PSF magnitude values to solve Z'_v and Z'_b for each chip.

2.1.3 Combination of deep and shallow exposures

After the final zero-points are calculated and applied to the photometry lists, the final stage of the data reduction is to merge photometry lists of different exposure time. This task was easily accomplished using a program written by Pat Durell. This program reads in the photometry list to be merged, and for all stars that appear in both lists selects only one to appear in the final list. The decision on which star to put in the final list is based on several criteria. The default choice is to take the star from the longer exposure, as it will typically have higher signal to noise. However, near the saturation limit of the deeper exposure, it is often unclear which star will have been more accurately measured. In this case the program examines the star on the deeper image for indications that it

was improperly measured, such as a unusually high error or bad χ^2 -value. If the star appears to be well measured in the deeper exposure, the values from the deeper exposure will be chosen. Conversely, if there appears to be a problem with the measurement on the deeper frame, the measurement from the shallower frame will be selected. Finally, if the star on the deeper exposure is clearly saturated, the program chooses the star from the shallower exposure.

2.2 CFHT Legacy Survey

The CFHTLS is an extremely ambitious project that will take over 500 nights of dark and grey time at the CFHT over the next five years ($\sim 50\%$ of the total dark and grey time available). The survey is divided into three subsurveys: the deep survey, the wide survey, and the very-wide survey. While both the wide and very wide surveys are fascinating projects, with many diverse science goals, the images obtained as part of these surveys will not be used in the thesis. Therefore, all remaining references to the CFHTLS will be specifically referring to the deep survey.

The CFHTLS-Deep survey has been allotted 202 nights over the duration of the survey. The primary science goal of CFHTLS-Deep is to map the distribution of galaxies out to high redshift and to detect thousands of type 1 supernovae. The survey consists of four single independent megacam fields of 1 square degree. Each field is imaged in the full set of CFHT's filters: u^* , g' , r' , i' and z' . In order of obtain the same approximate limiting magnitude in each band, the exposure time must vary from filter to filter. This is to compensate for the varying sensitivity of the camera, Strehl ratio, and sky brightness in the various bands. The final exposure times are intended to be: $u^* - 33$ hours, $g' - 33$ hours, $r' - 66$ hours, $i' - 132$ hours, and $z' - 66$ hours. The survey will reach a projected limiting magnitude of ~ 28 in all five bands. The fields were selected to be at high Galactic latitude to avoid dust and disk stars, making them perfectly suited to the needs of this project. The coordinates and reddening values of the four fields, named D1,D2,D3 and D4, are listed in the table 2.1. The positions of the fields are shown schematically

Name	RA (hr:min:sec)	Dec (deg:min:sec)	l	b	E(B-V)
D1	02:26:00	-04:30:00	172°	-58°	0.02
D2	10:00:29	+02:12:21	237°	+42°	0.01
D3	14:19:28	+52:40:41	96°	+60°	0.01
D4	22:15:31	-17:44:06	39°	-52°	0.03

Table 2.1: Coordinates of the center of the CFHTLS-Deep fields. The excess colour is not constant over the field. The value quoted is a typical value for each field, but there are variations of ~ 0.01 mags. These value are derived from Schlegel’s dust map [35].

in figure 2.1.

2.2.1 Reduction

An integral part of the CFHTLS is the pipeline to reduce the data, making it easily used by a wide cross section of the astronomical community, from astronomer that work primarily at other wavelength to theorists. Every level of the data is (or will be) available to the community, from raw images, through preprocessed images, to stacked images and ‘data products’ such as photometry lists. This is made possible through several facilities. preprocessing is performed at CFHT with the Elixir pipeline. The images are stacked, and reduced at TERAPIX (Traitement Élémentaire, Réduction et Analyse des PIXels de megacam). Finally, images and data products are distributed through the Canadian Astronomical Data center (CADC).

Elixir

Within several weeks of the end of an observing run raw images and preprocessed images are available to the astronomical community on-line through the CADC. The preprocessed images are pipeline processed with Elixir. Elixir applies dark images, flat fields, and bias images to every image. As more and more data accumulates, the flat field

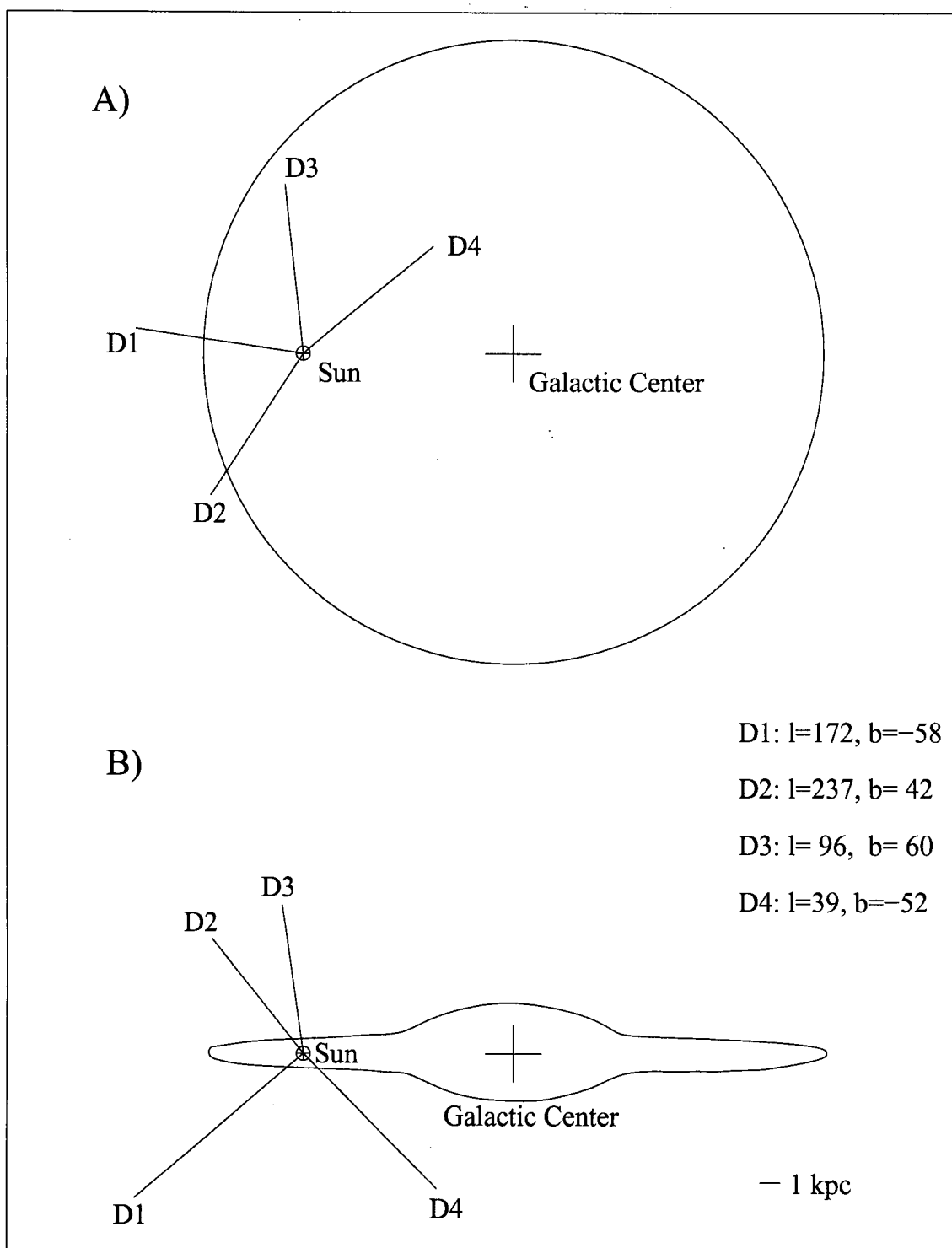


Figure 2.1: The locations of the fields D1, D2, D3, and D4. In frame A) the view is from the Galactic pole, with $l=0$ to the right. In frame B) the view is from the Galactic plane again with $l=0$ to the right

images may be averaged to construct a 'superflat'. This allows the zero-points for each image to be determined very accurately for every chip in Megacam. Zero-point are now known to < 0.01 magnitudes. However, Elixir does not release any combined images, or data products.

Terapix

TERAPIX is an astronomical data reduction center dedicated to the processing of extremely large data flows from digital sky surveys. TERAPIX is located at IAP (Institut d'Astrophysique de Paris). The Terapix organization is responsible for making the data available and useful for people without the knowledge, time, or computing power necessary to perform their own reductions. Terapix will stack all images using the Bertin's SWarp program. This will give the images their advertised depth. Furthermore, it will reduce the stacked images, creating photometry lists for each of the images. The image reduction will be performed by a pipeline based on Bertin's SExtractor and PSFex. Terapix has yet to release data, but is due for its first data release very soon.

University of Victoria

Megacam images are very large, and the process of stacking images is very time consuming. Terapix has been plagued by delays, and has not yet released stacked images. Fortunately, the Department of Physics and Astronomy at the University of Victoria has a group working on galaxies in the CFHTLS-Deep fields. The data reduction at this group is led by Stephen Gwyn. Stephen Gwyn generously provided me a with copy of his stacked, Elixir processed, images. High photometric precision is not required for this project. As long as the photometry is accurate to within the size of a typical bin we are unaffected by photometric errors. Because of this, aperture photometry was sufficient, and point-spread photometry was not necessary. The images were reduced using the fast and highly automatic software package SExtractor. The images were obtained as multi-extension FITS (MEF) files. This means that one file contained the images for all 36 chips. With most software packages, MEF files have to be decompressed, and each

extension analysed individually. SExtractor can analyse MEFs directly, without decompressing the file. After the process was scripted, the processing of all 36 chips in a field in all filters took approximately 90 minutes on a desktop PC. This is an impressive accomplishment considering that that entails approximately 2×10^6 accurate photometric measurements.

2.2.2 Star-galaxy separation

Although the main goal of the CFHTLS-deep is to detect galaxies, the survey will inevitably image a fascinating set of stars. The utility of this data set in star-count modeling is limited not only by the limiting magnitude of the survey, but also by our ability to distinguish between stars and galaxies. Because of the difficulty of distinguishing between stars and galaxies at faint magnitudes, the data used for this study will be several magnitudes brighter than the detection limit. This means that the completeness will be close to 100%. There are several methods used to distinguish stars from galaxies. Each method has its advantages and disadvantages.

The simplest methods use a distinctive feature to distinguish stars from galaxies in some 2-d parameter space. These methods include magnitude-isophotal area[25], magnitude-peak intensity[13], and magnitude-surface brightness[10]. These methods typically work well at bright magnitudes. However, these methods do not use all the information contained in the brightness profile, and hence are limited at fainter magnitudes. More sophisticated methods such as the Sebk classifier[34], the r^{-2} moment[14], the Q classifier[19], and the ψ parameter[20], use more of the information in the intensity profile, but are not found to be robust when confronted with merged objects or crowded fields.

By viewing objects as vectors of parameters, the separation of star and galaxies can be thought of as the definition of a hypersurface that separates the populations effectively in a multi-dimensional parameter space. This is the philosophy used in Emanuel Bertin's stellerity index [3], which is incorporated directly into SExtractor. The hypersurface

dividing stars from galaxies is determined using a neural network consisting of one input layer, one hidden layer, and one output layer. A neural network is only as good as its training. The neural network used to calculate stellarity in SExtractor was trained by Bertin in a magnitude regime where star counts are approximately equal to galaxy counts. This means that the stellarity index is most accurate from $18 > V > 22$ [3]. For objects brighter than the $V \sim 18$ limit, it is quite simple to distinguish stars from galaxies. The more challenging regime is for objects fainter than $V \sim 22$.

The next several paragraphs I describe the steps in the separation of stars from galaxies in the CFHTLS-D4 field (chosen because it has the highest number of stars). Shown in figure 2.2 is a CMD of all the objects the CFHTLS-D4 field. There are 2.7×10^5 objects in the diagram.

For the purposes of this study we were concerned only with halo stars. In order to distinguish halo stars from disk stars we take advantage of their different metallicities. Stars with a significant metal content, i.e. disk stars, have far more absorption lines in their atmospheres than metal-poor stars, i.e. halo stars. This has the implication that the total flux emitted at short wavelengths by disk stars is less than that emitted by halo stars. This results in redder colours for disk stars. A diagram of the theoretical distribution of disk stars and halo stars is shown in figure 2.3. In all colour-colour spaces and the colour-magnitude space denoted in this figure, halo stars and disk stars separate. For our study we chose the boundaries $g' < 24$, $g' > 18$, $(g' - r') < 0.8$ and $(g' - r') > 0.1$. This space was chosen as the largest area dominated by halo stars with small contamination by thick disk stars. Stars are point sources, and therefore follow a tight magnitude-half light radius relation. If the stars are faint enough that saturation effects, such as potential well overflow and bleeding, are not important, their half-light radii will be independent of the magnitudes, and should be close the telescope PSF. This creates the tight sequence that can be seen for half-light radii smaller than $0.9''$. For magnitudes brighter than $g \sim 22$ we can easily separate stars from galaxies using this sequence. A magnitude – half light radius diagram is shown in figure 2.4. Figure 2.5 shows a smaller area of colour – magnitude space with only objects that satisfy the

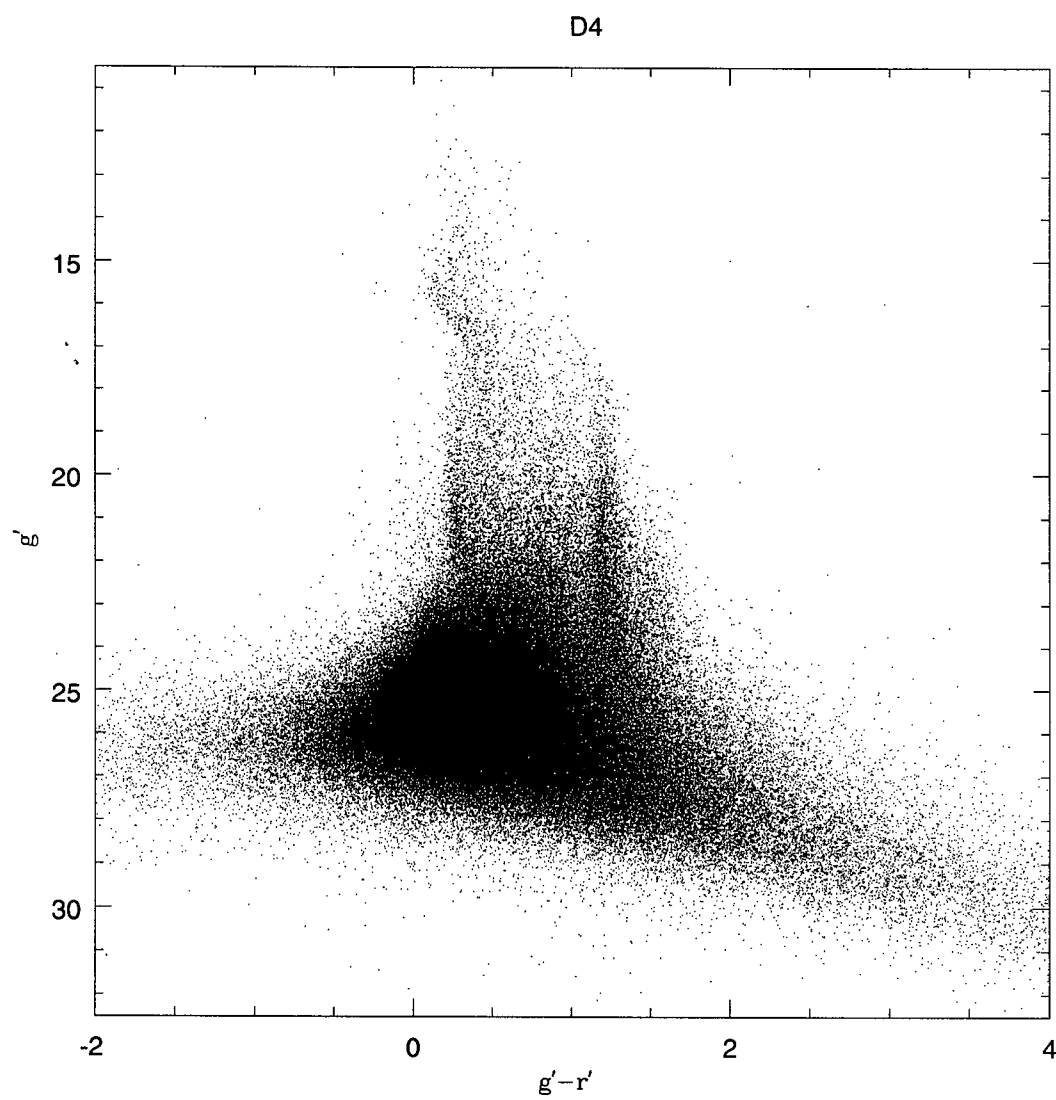


Figure 2.2: A CMD of the 2.8×10^5 objects present in the field CFHTLS-D4.

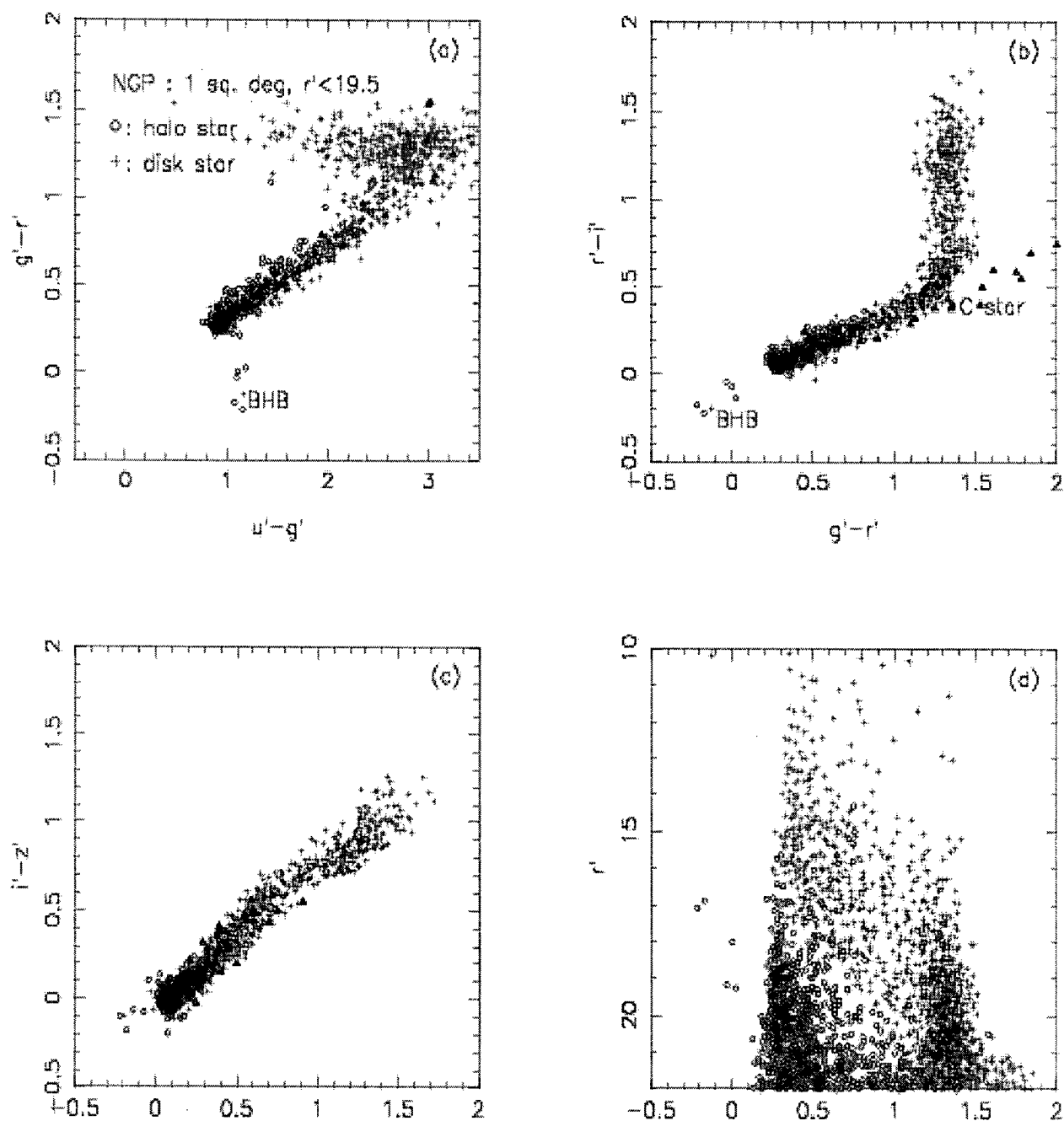


Figure 2.3: A figure taken from Fan 1999. In all four frames, disk stars are shown as '+' while halo stars are shown as 'o'. In frame d, notice that at magnitudes brighter than $g \sim 18$ the space is dominated by disk stars. At magnitude $g > 18$ the disk and halo populations separate in colour. The halo stars are of lower metallicity and are therefore bluer..

half-light radius $< 0.9''$ cut.

Many quasars and compact galaxies satisfy the colour-magnitude space selection and have small half-light radii. Fortunately, quasars and compact galaxies typically occupy a different region of colour-colour space. A theoretical plot showing the positions of stars, compact emission line galaxies, quasars, and white dwarfs is shown in figure 2.6. An observed colour-colour plot is shown in figure 2.7. Figure 2.8 shows a colour magnitude diagram after quasars and galaxies have been removed with a colour-colour cut. Note that there are almost no objects bluer than the main sequence turnoff. If analysis is restricted to the magnitude brighter than $g' = 24$ then these cuts are sufficient. We can do slightly better with aggressive pruning in colour-colour space. Halo stars occupy a strict region of parameter space. We can safely reject any object that does not lie close to the sequence. Figure 2.9 shows the selections in colour-colour space. Figure 2.10 show the CMD of the resulting selections in colour-colour space.

One can now take advantage of the stellarity index. Up to this point we can be quite sure that we have not cut any stars from our data set. An examination of where our objects lie on the magnitude-stellarity plane shows that the vast majority of objects brighter than $g' = 24$ have a stellarity, s , greater than $s = 0.97$. This is interesting for the following reason: when trying to separate stars from galaxies the stellarity index is often the only figure of merit examined. A much less stringent stellarity cut is typically employed. This diagram shows that in doing this one may be selecting compact “star like” galaxies. We can now choose to set our limiting magnitude at the elbow of the stellar sequence in the stellarity-magnitude diagram. This occurs at approximately $g' = 24$. This is shown in figure 2.11. A small number of objects have very high stellarity and small half-light radius in one band, but not in others. We take advantage of the multi-colour aspect of the CFHTLS-Deep by requiring that the above criteria are satisfied in every filter.

Every magnitude gained deeper than $g' = 24$ will yield a windfall of stars. Unfortunately in this regime galaxies and stars both appear as unresolved point sources in ground based images. The extremely small PSF of HST would allow one to probe deeper, but

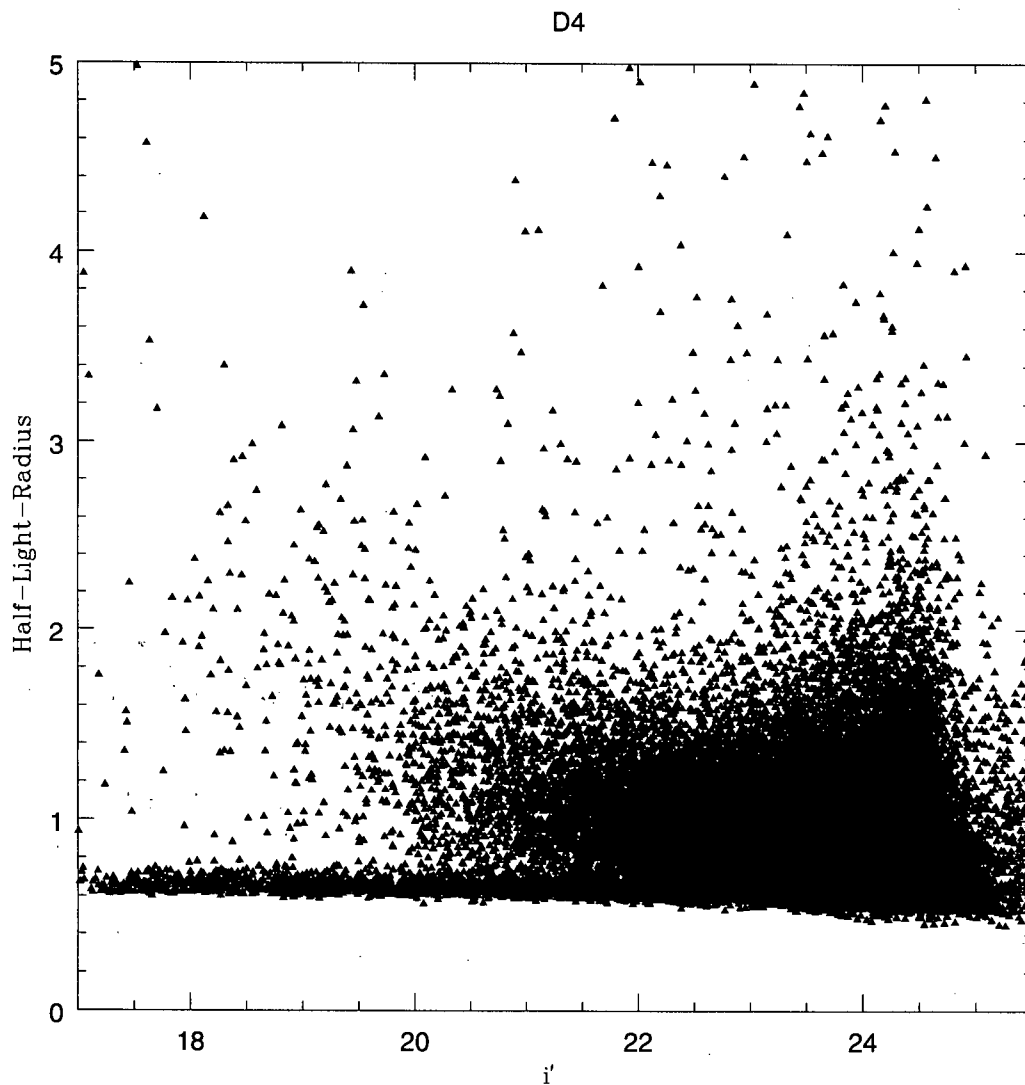


Figure 2.4: A diagram of half-light radius versus magnitude. There is a clear stellar sequence at half-light radii smaller than $0.9''$. There are $\sim 4 \times 10^3$ objects in the stellar sequence brighter than $i' = 22$ and $\sim 8 \times 10^3$ objects with half-light radius smaller than $0.9''$ in total.

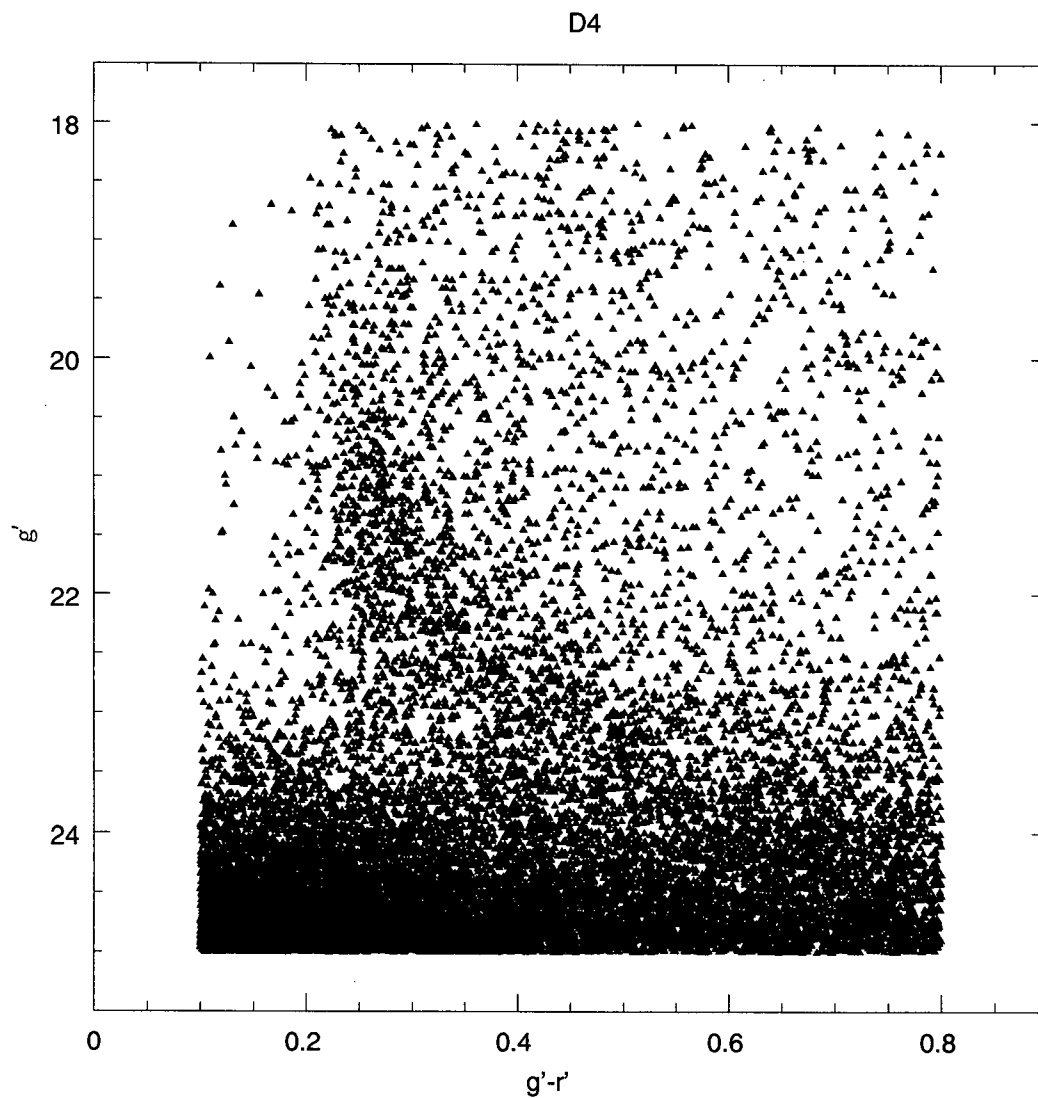


Figure 2.5: A CMD of all objects satisfying the half-light radius $< 0.9''$ cut. There are $\sim 8 \times 10^3$ objects in this diagram.

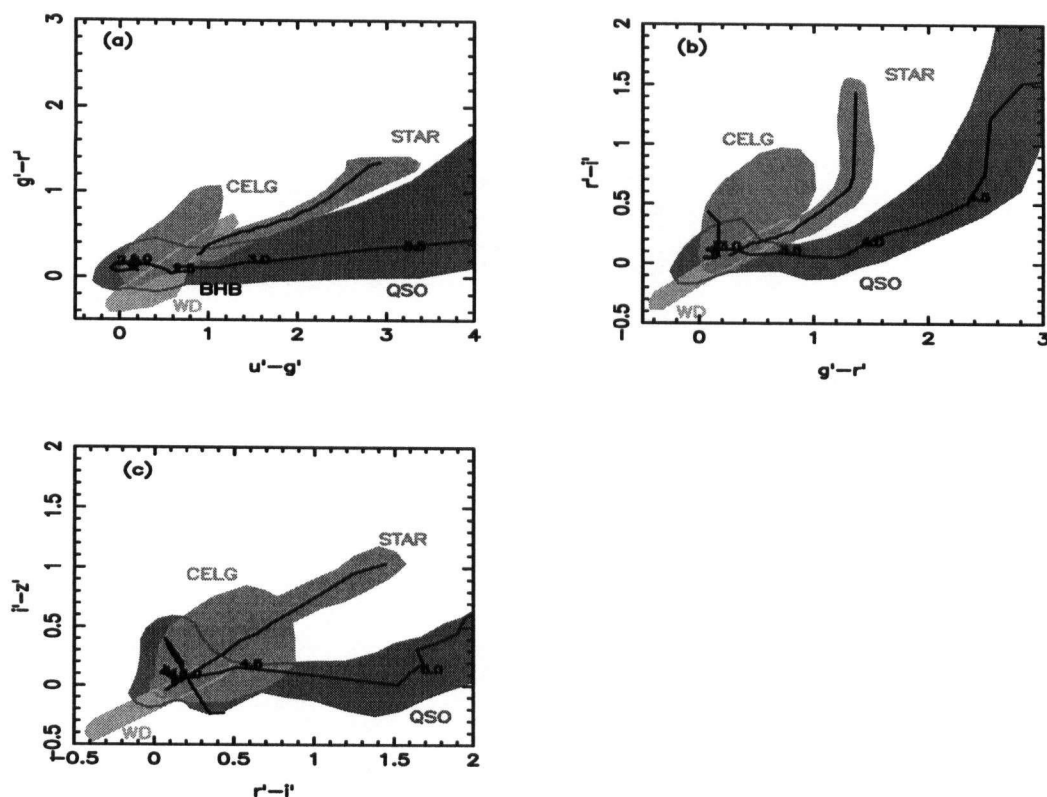


Figure 2.6: Figure taken from Fan 1999. A colour-colour plot showing the theoretical positions of compact emission line galaxies (CELG), quasars (QSO), stars, blue horizontal branch stars (BHB), and white dwarfs (WD). Note that although the quasar region is very large, the number of quasars with blue $u^* - g'$ colours is much higher than the number of red $u^* - g'$. Elliptical galaxies and quiescent spiral galaxies are not shown on this plot, but are cleanly separated from the stellar sequence.

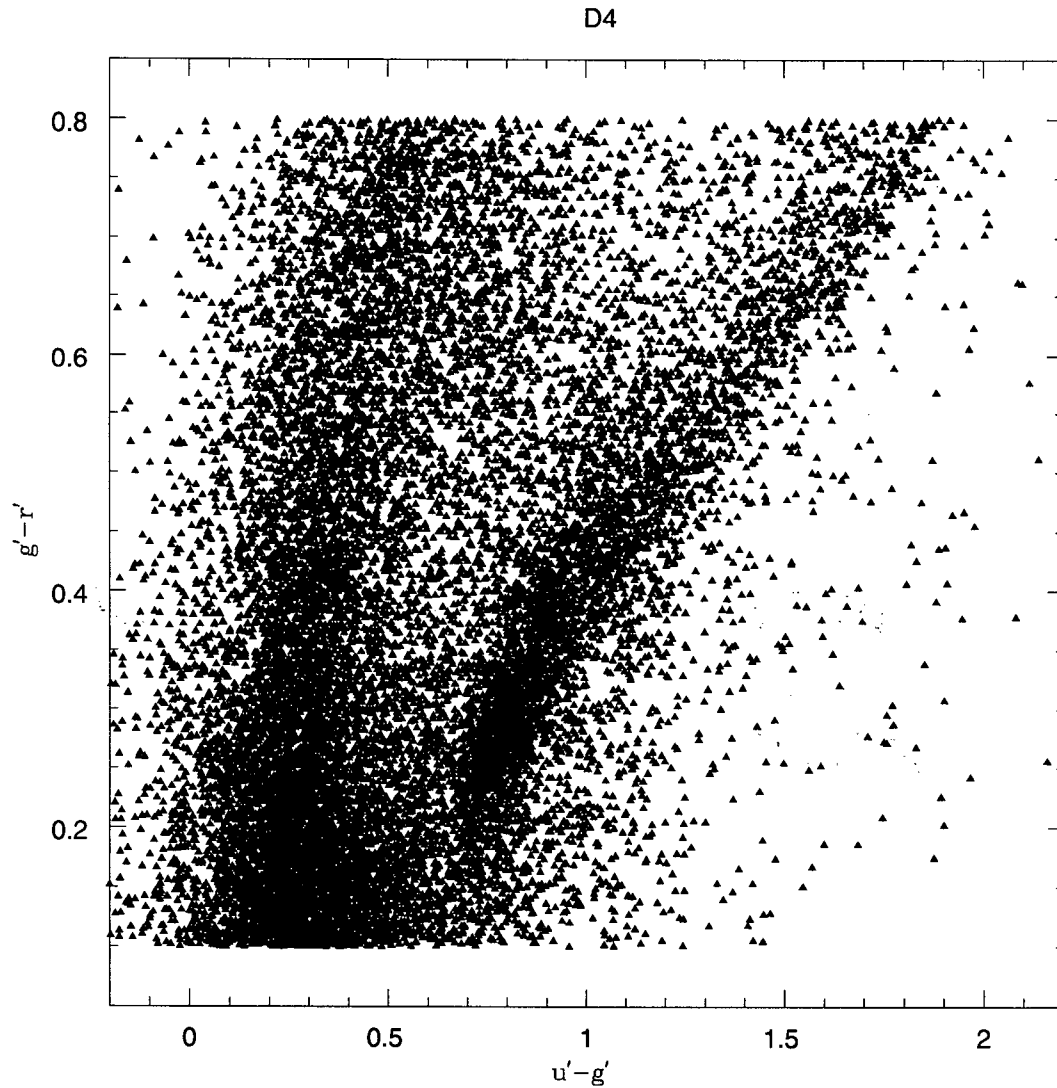


Figure 2.7: A colour-colour plot of objects with a half light radius less than $0.9''$. The stellar sequence is clearly seen on the right of the diagram. Extragalactic objects occupy the region blue-ward of $u^* - g' = 0.6$.

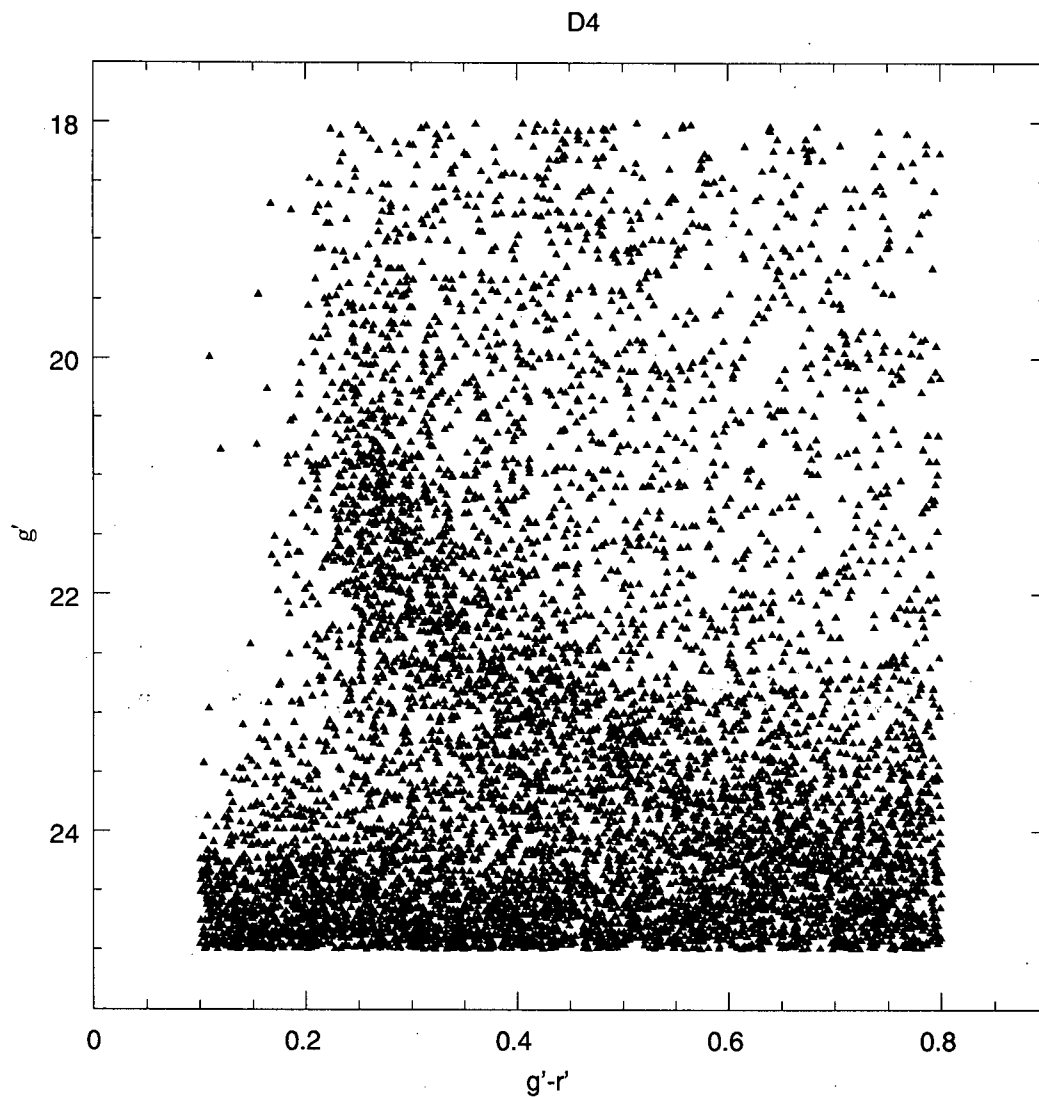


Figure 2.8: A CMD of objects that satisfy the colour cut of $u^* - g' > 0.6$ and the half-light radius cut. There are almost no objects blue-ward of the main sequence turnoff at magnitudes brighter than $g' = 24$. This indicates that we have removed the vast majority of extragalactic objects brighter than $g' = 24$

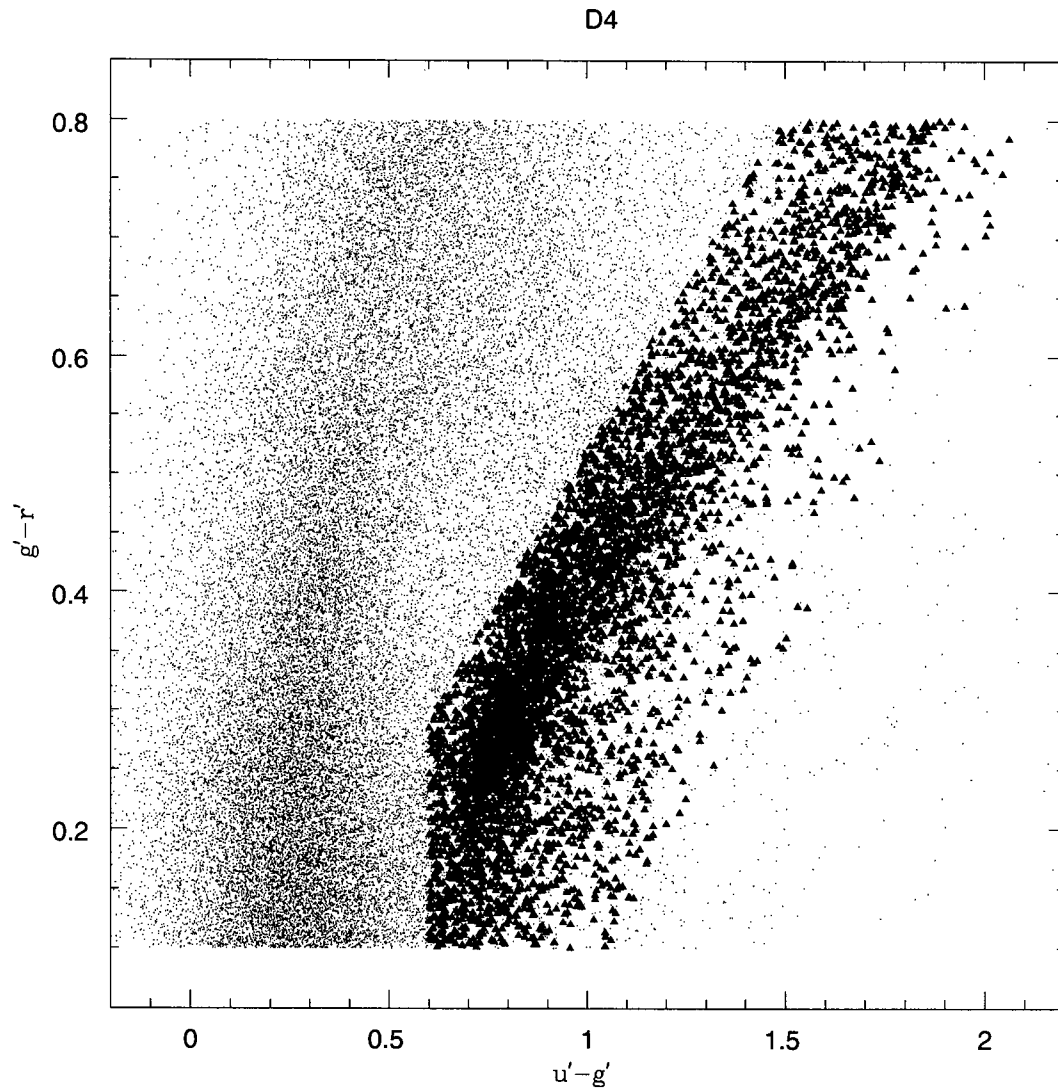


Figure 2.9: A colour-colour diagram showing the selection criteria used in this study. This is designed to follow the obvious stellar sequence as closely as possible without removing stars that may have been poorly measured in one filter.

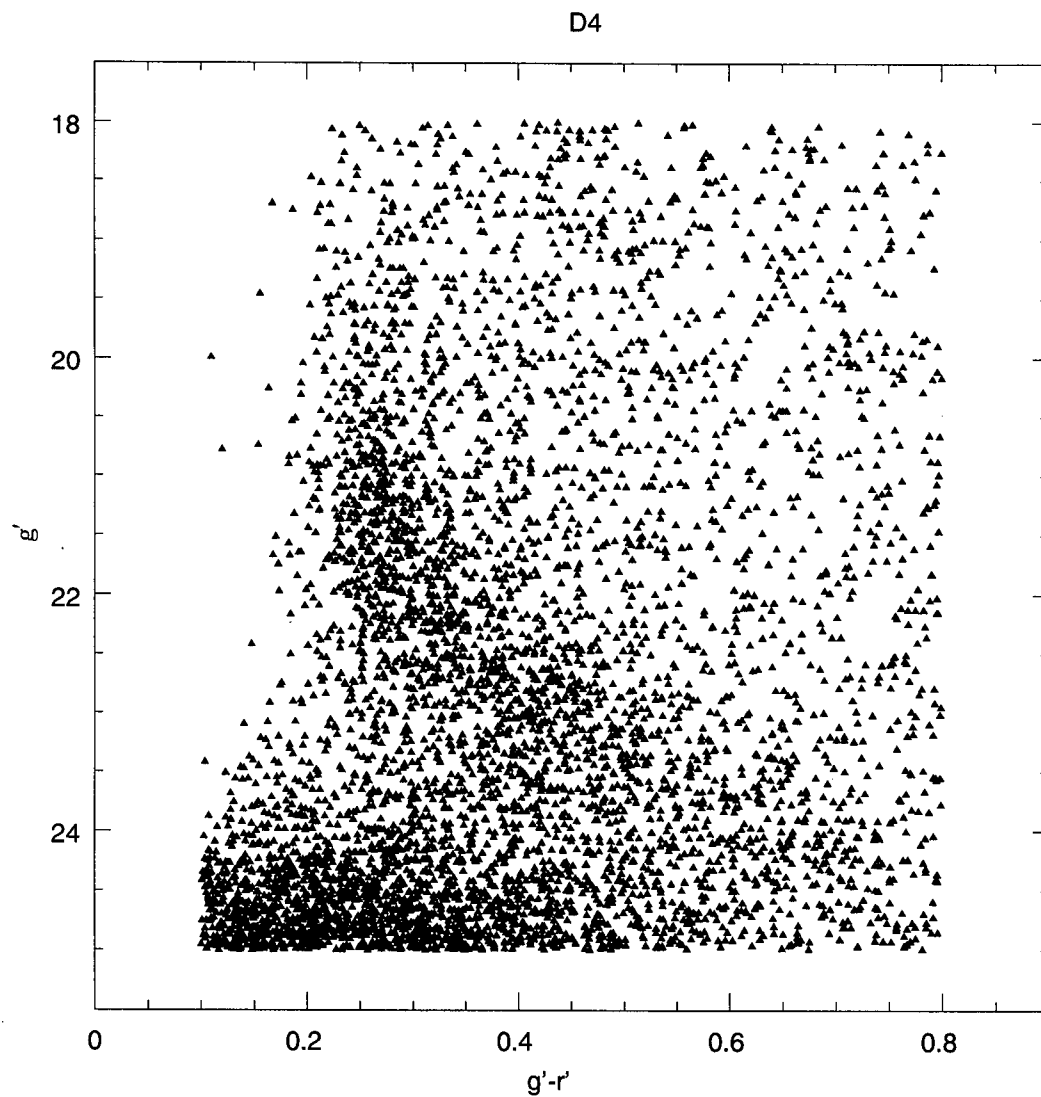


Figure 2.10: A colour-magnitude diagram like figure 2.8, but showing the set of objects satisfying the more stringent colour-colour selection criteria shown in figure 2.9.

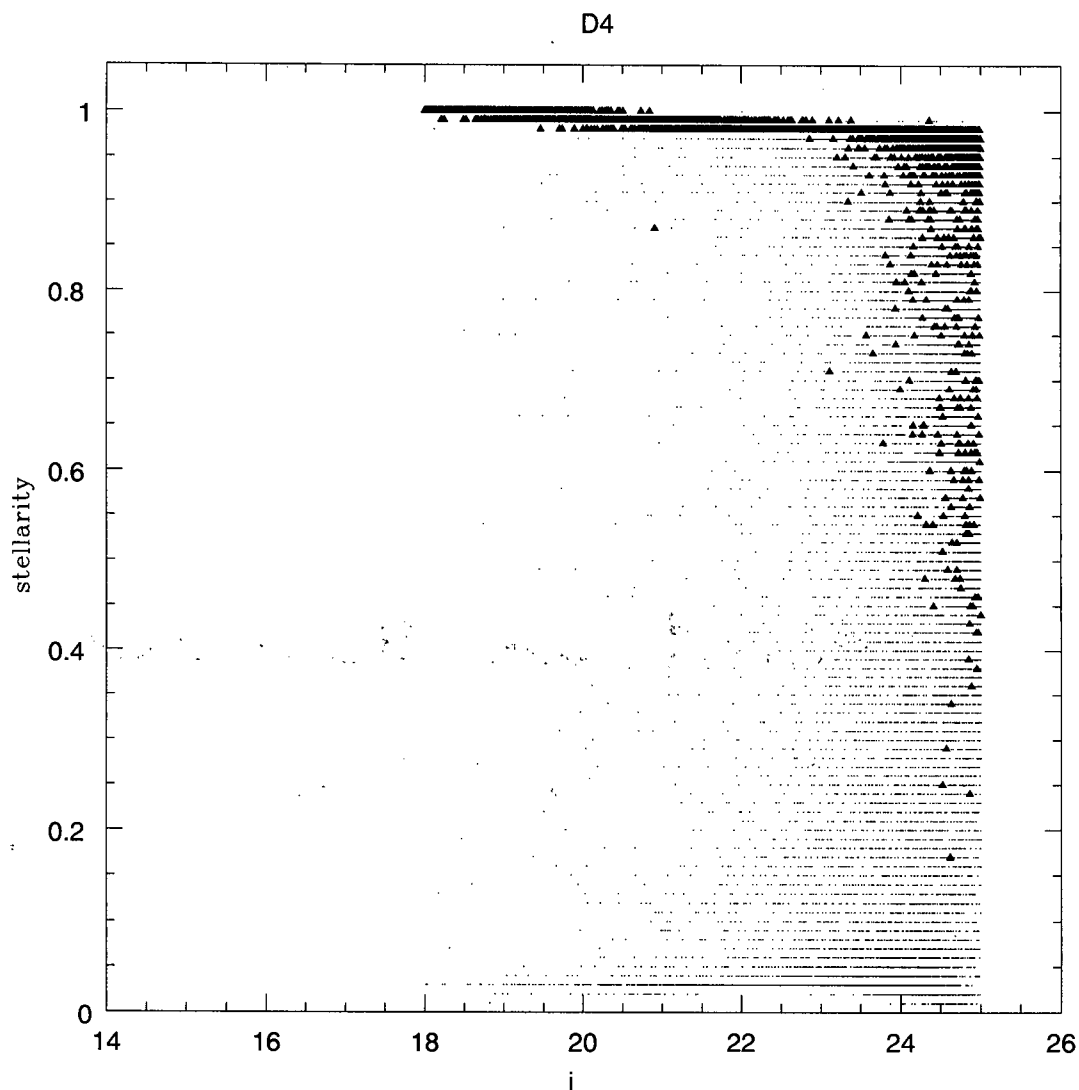


Figure 2.11: Stellarity as a function of magnitude. All objects are shown in black, and points satisfying the aforementioned criteria are shown in blue. Note the elbow in the distribution of stars at $i' \sim 24$ and $s \sim 0.95$. This marks the end of the range where stellarity is a useful measurement.

the field of view of HST is small. Furthermore, the increase in the number of galaxies overwhelms the increase in the number of stars. Finding the one star in thousands of galaxies becomes a search for a needle in a haystack, and contamination is inevitable. Until there are space-based telescopes equipped with cameras that have large fields of view, magnitudes of $g \sim 25$ may be the limit at which star-count studies are practical. CMDs of the four fields (with objects in the desired colour-magnitude space subjected to the above selection criteria) are shown in the figure 2.12. Note the differences between the CMDs from the different lines of sight in the parameter space denoted with a box. Because of the different Galactic coordinates of the fields these lines of sight pass through different sections of the various Galactic components.

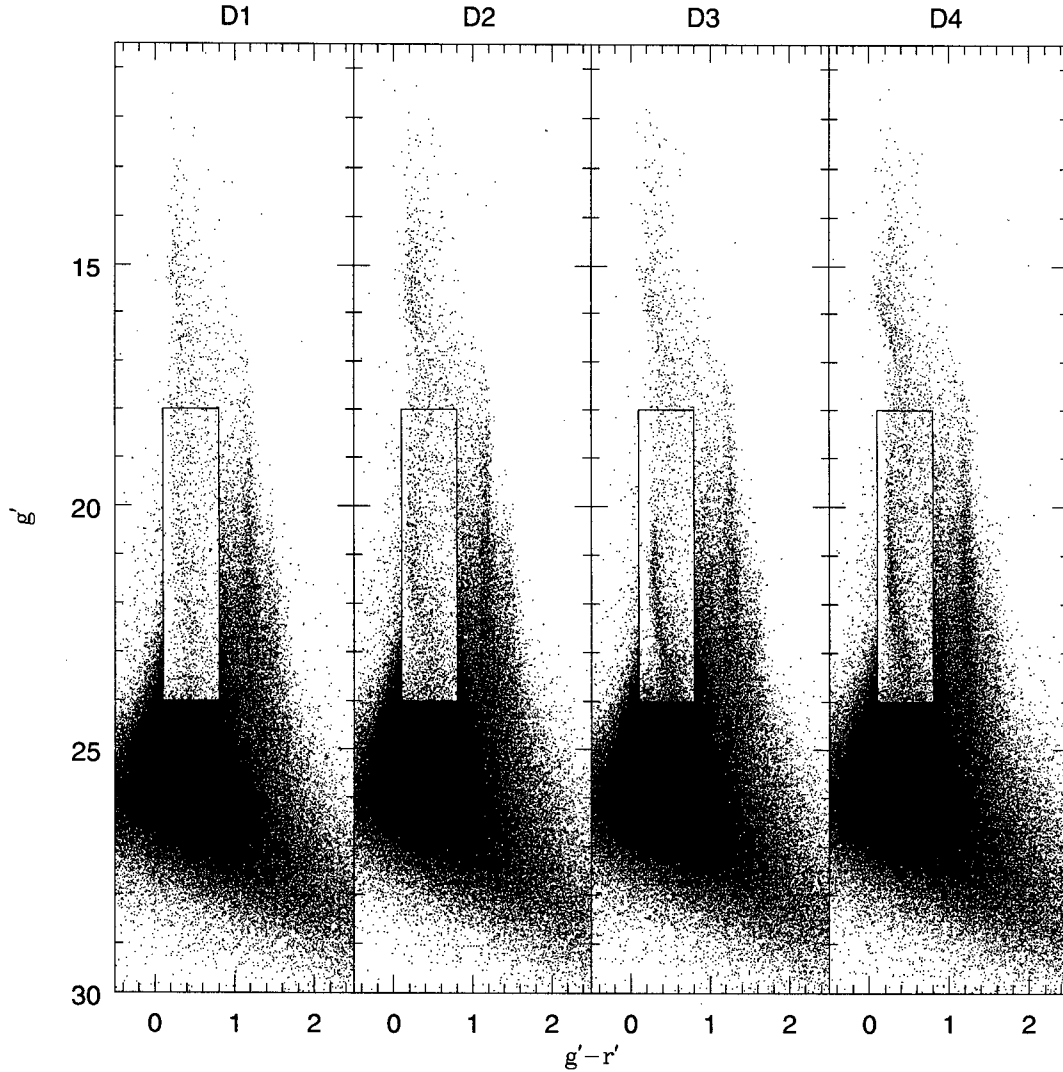


Figure 2.12: A CMD of all the objects present in the field CFHTLS-D1, CFHTLS-D2, CFHTLS-D3, CFHTLS-D4. The colour-magnitude space analysed in the project is denoted with a box. This area was selected to be the region of colour-magnitude space dominated by halo stars. Objects in this area are subjected to a stellarity cut, half-light radius cut, and a colour-colour cut. There are 2.7×10^5 objects in each panel. There are 2.2×10^3 , 2.8×10^3 , 3.9×10^3 , and 1.5×10^3 objects contained within the boxes in D1, D2, D3, and D4 respectively.

Chapter 3

The models

The degeneracy between the distance to a star and its intrinsic luminosity is at the heart of the challenge of determining the form of the Galaxy. The fact that it is impossible to distinguish a local M-dwarf from a distant red giant from photometry alone creates a degeneracy between the physical shape of the Galaxy and the types of stars that inhabit the Galaxy. Given a hypothetical form of the Galaxy, it is a relatively straightforward task to simulate an artificial colour-magnitude diagram. Unfortunately, the reverse is not true. There are many different combinations of parameters that can create virtually identical CMDs, making the direct mapping from CMD to Galactic form impossible. This fact necessitates a more statistical approach to the problem.

The most natural approach to simulating CMDs is to use Monte Carlo simulations. A Monte Carlo simulation uses a sequence of random numbers to sample stochastically a given probability distribution. Using a Monte Carlo simulation it is possible to create a photometry list – the same form of data that one obtains from analysing CCD images. Monte Carlo simulations are simple to use, and can incorporate subtle features, such as photometric errors and incompleteness.

Monte Carlo simulations have several drawbacks. First, the results they give are stochastic – the output of the model is dependent on the initial random seed. This is the very quality needed for some applications. For others, especially those dealing with relatively small numbers of simulated objects, the stochastic nature of the simulations is just a source of noise. For our project, we are counting the number of stars observed in bins. In order to resolve features distributed across colour – magnitude space we must make those bins small. Due to the large number of bins, we have a small number of stars in any one bin, and are therefore dominated by Poisson noise.

This means that if we expect several stars in a bin, variations on the order of 100% for different random realizations are not uncommon. The most common methods to overcome the inherent noise involved in Monte Carlo simulations is to run the simulations many times. This is done by either casting several simulations with different random seeds, or by generating many more points than are needed and then statistically scaling the results back. The second drawback is linked to the first – Monte Carlo simulations are computationally very expensive, and for some applications, prohibitively slow.

The negative features of the Monte Carlo technique are very apparent for our application. It takes minutes for the simulation of one CMD using modern desktop PCs. This begs the development of an alternate method. The method used in this project was to create a map of probability contours from the probabilities directly, rather than to stochastically sample probabilities, as in a Monte Carlo approach. The main drawback of this method is that it is impossible to create a photometry list. One must directly simulate a probability map. Furthermore, the inclusion of stochastic effects, such as photometric error, were far more difficult to make part of this simulation.

The implementation of these two techniques will be discussed in the next sections. A flow diagram for both the aforementioned methods is shown in figure 3.1.

3.1 Monte Carlo Simulations

The Monte Carlo code used for this project, MILKYWAYMC, was inspired by the pioneering work of Bachall and Soneira in the 1980's. In this model[1], the Galaxy is composed of three components: a young thin disk that contains most of the stellar mass of the Galaxy, an intermediate thick disk, and an old spherical halo. Whereas the Bachall & Soneira code made use of an empirical luminosity function, MILKYWAYMC uses theoretical stellar evolutionary tracks and star formation histories to generate the luminosity distribution. MILKYWAYMC gives us the ability to constrain the star formation history of the Galaxy, as well as the IMF of the stars within the Galaxy. The following section is a description of the steps the code goes through to create an artificial photometry list.

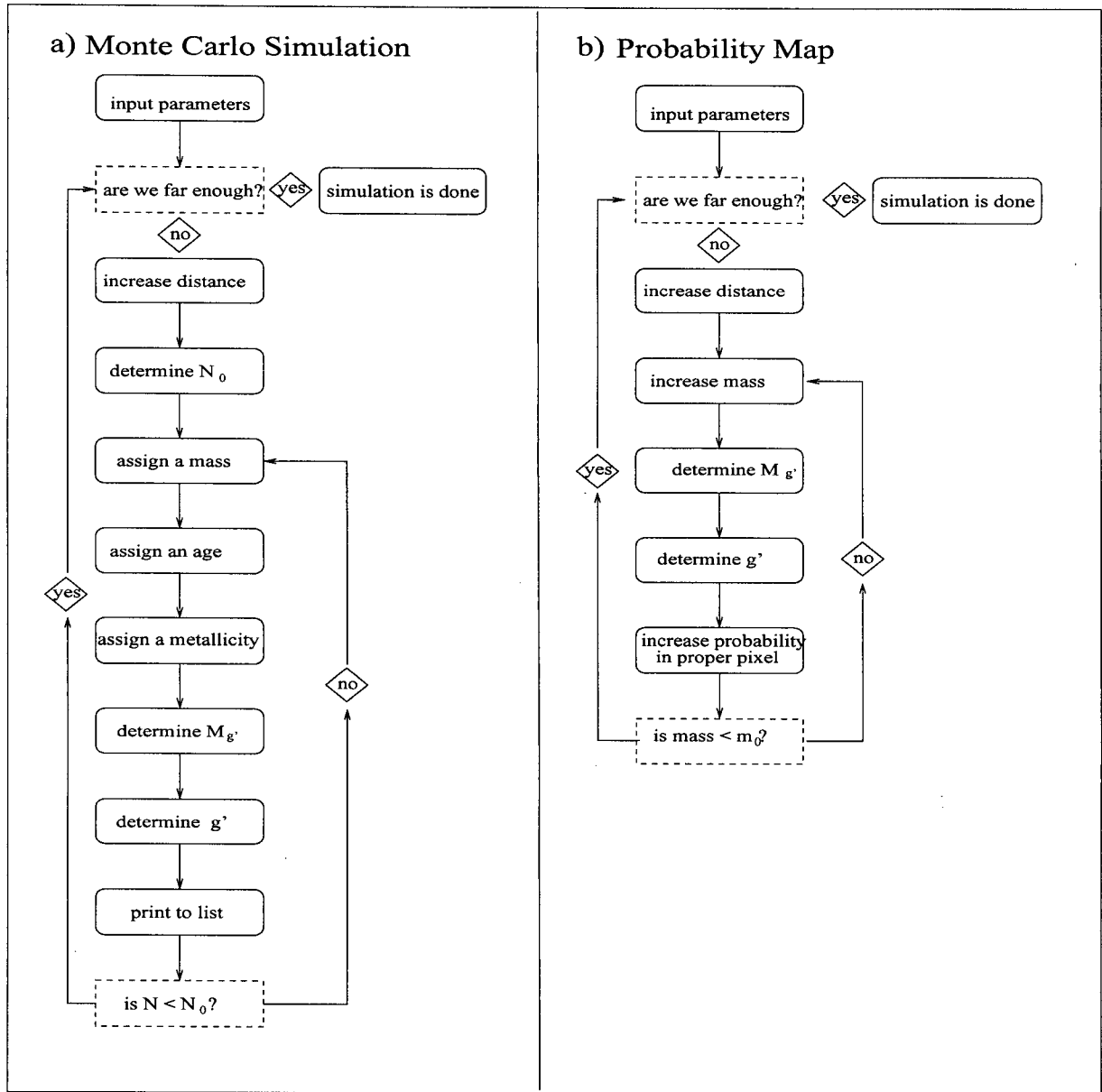


Figure 3.1: A flow diagram for the Monte Carlo and probability map methods. The process for dealing with binaries is not shown, but occurs concurrently with the main loop for both procedures. For the Monte Carlo method, a random number is drawn, and if this number is lower than the binary fraction, a second mass is assigned. The fluxes of the stars are added, and the new magnitude and colour calculated. For the probability map, a sequence of diminishing probability is added above the main sequence up to $\Delta mag = 0.75$ – the maximum deviation from the main sequence for a binary star (equal mass binary).

1. The first step in the Monte Carlo simulation is the input of parameters. Parameters of the observations (field of view and limiting magnitude), specifics of the spatial distribution (Galactic coordinates, local density and scale length) and specifics for each thick disk, thin disk, and halo (star formation history, metallicity distribution and binary fraction) must all be input to the code. For our project, only the halo was simulated. This decreases the number of input parameters substantially. We can reasonably model the halo with one metallicity and one burst of star formation. Due to the long main-sequence lifetime of the low mass stars in the halo, the results are relatively insensitive to the age of the halo population. Ages from 10 Gyr to 14 Gyr produce similar results. We choose the metallicity to match that of metal-poor globular clusters.
2. The main section of the code involves stepping through distance moduli until the edge of the Galaxy has been reached. Given the location of the Sun in the Galaxy, the supposed spatial distribution of the halo, the local density of halo stars, and a heliocentric distance, we calculate the corresponding volume and the number of stars, N_0 , of each population brighter than a limiting absolute magnitude, M_0 , expected. This limiting magnitude is chosen to agree with the limiting magnitude of the Hipparcos mission to facilitate comparison with the Hipparcos data set. A Monte Carlo is then employed to choose the masses of stars stochastically. The mass selection works in the following manner: The value of C is calculated such that

$$C \int_{m_{low}}^{m_{high}} m^{-\alpha} dm = 1. \quad (3.1)$$

3. A random number generator then picks a number, R , and the mass of the star, m_0 , is calculated such that

$$C \int_{m_{low}}^{m_0} m^{-\alpha} dm = R. \quad (3.2)$$

4. A random number is drawn to decide if the star has a binary companion. Again, m_0 is calculated for the companion star.

5. The metallicity and age of the star(s) are determined in a similar manner. For this thesis, the metallicity and age were held constant, so this step could be omitted. We adopted an halo age of 12 Gyr and a halo metallicity similar to metal poor globular clusters, $[Fe/H] = -2.0$.
6. Using a star's mass, age, and metallicity, its magnitude in various filters is calculated from a set of homogeneous evolutionary tracks. These tracks were provided by the astronomy group at the University of Pisa. These tracks have evolutionary stages from Zero Age Main Sequence (ZAMS), through post main sequence evolution, to supernova and white dwarf stages.
7. Photometric errors are added to the star's magnitude as a function of magnitude.
8. Stars are picked as described in steps 3 to 6 until there are N_0 stars with an absolute magnitude brighter than M_0 .
9. Steps 2 to 8 are then repeated for each distance modulus until the entire Galaxy is simulated.

A sample of a CMD created from a simulated photometry list is shown in figure 3.2.

3.2 Probability Map

The code used to make the probability maps had the same basic form as the Monte Carlo, but with some important differences – the most important being that it is unnecessary to calculate integrals to determine specific values of mass thereby dramatically reducing the computational cost. The following section is a description of the steps the code goes through to create a colour-magnitude probability map.

1. As with the Monte Carlo simulation, the first step of this code is to input various parameters. However, in this case, the probability map remains unnormalized until the last stage of the code. This means that the probability map is independent of

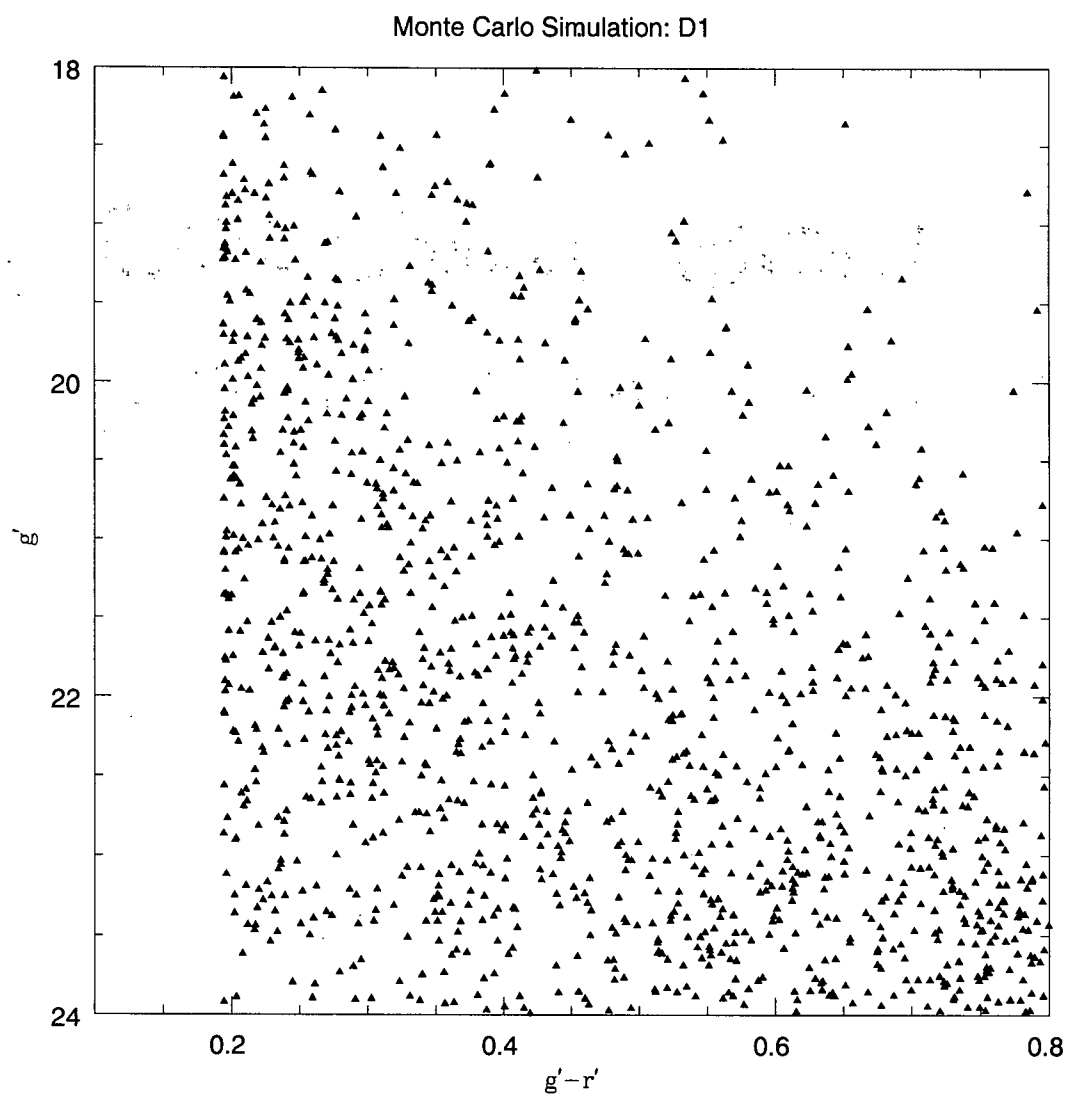


Figure 3.2: A CMD created from a Monte Carlo simulation of the Galactic Halo.

local density and field of view of the camera. When comparing a simulated probability map with observed data, the map is normalized to the number of observed stars. This means that it is impossible to constrain the local density of stars via this method.

2. Again, the bulk of the code involved stepping through distance moduli until the edge of the Galaxy was reached. Like step 2 in the previous list, we calculate a number, N , based on the Sun's Galactocentric distance, the supposed spatial distribution, and the calculated volume element. Because the probabilities are unnormalized, this number does not have a physical meaning. It simply serves to scale the probabilities with distance and hypothesized stellar density. Because we cannot discover the local density of halo stars directly using this code, the best fit for only the four other parameters will be determined with this method. The normalization will be found using the Monte Carlo technique.
3. The next step differs the most from the Monte Carlo approach. Whereas in the Monte Carlo approach masses are stochastically assigned, in this approach probabilities, $P(m)$, are calculated for *every* mass according to the equation

$$P(m) = m^{-\alpha}. \quad (3.3)$$

4. As with Monte Carlo, colours and magnitudes are calculated via stellar evolutionary tracks.
5. The product of $N \times P(m)$ is stored in the appropriate pixel for each mass.
6. Steps 2 through 5 are repeated over the appropriate range of distance moduli.
7. Finally, the entire array of pixels is multiplied by a constant to ensure the sum over all the pixels is equal to the number of stars in the observed field.

Probability maps of the expected stellar distribution created in this manner are shown in figure 3.3. The differences in the shape of the contours is accounted for by the different

number densities at various distance moduli. The number density as a function of density for the four lines of sight is shown in figure 3.4.

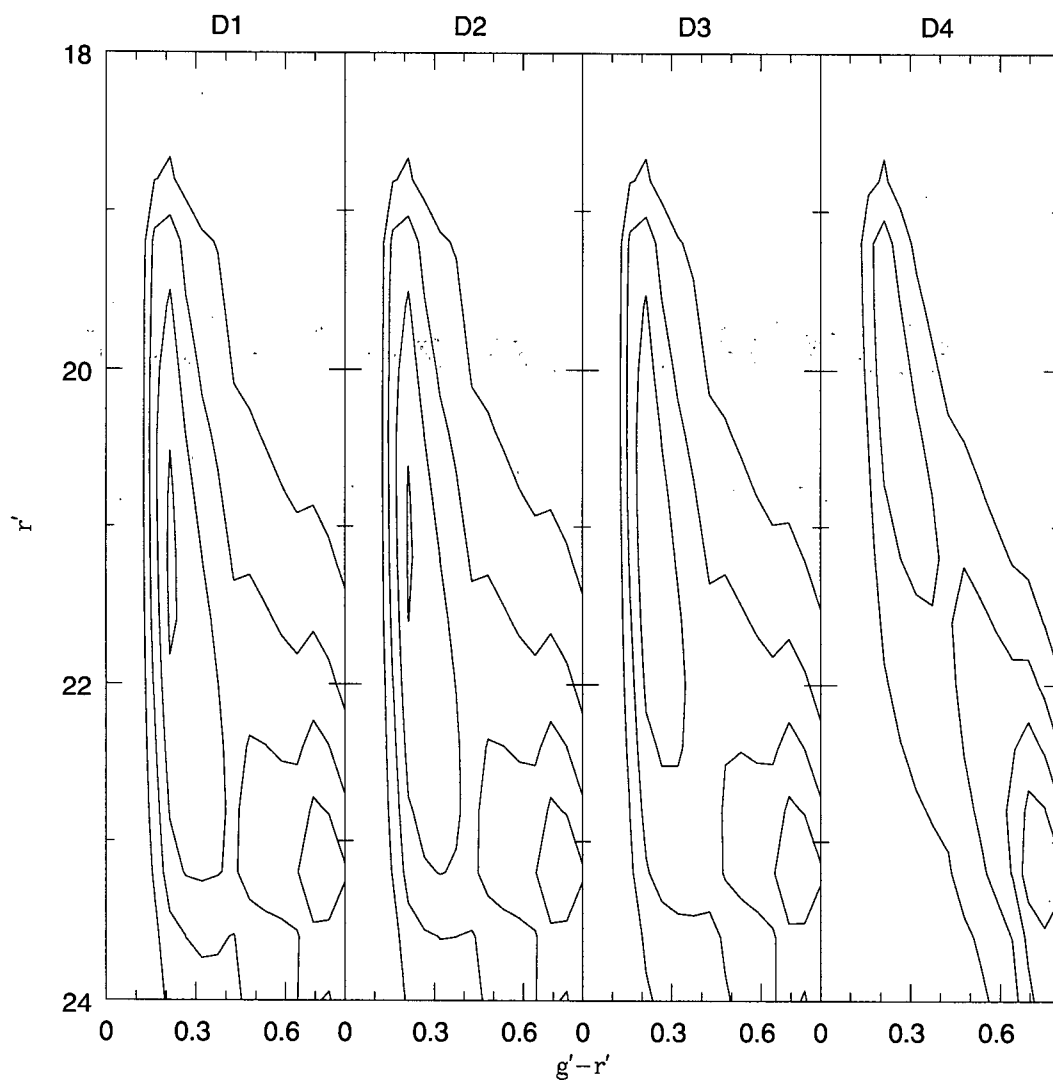


Figure 3.3: A probability map created for the fields D1 ($l=172^\circ, b=-58^\circ$), D2 ($l=237^\circ, b=42^\circ$), D3 ($l=96^\circ, b=60^\circ$), and D4 ($l=39^\circ, b=-52^\circ$). The peaks for D1, D2, D3, and D4 are in different locations due to the different number of stars expected at various distance moduli for the various lines of sight as shown in figure 3.4.

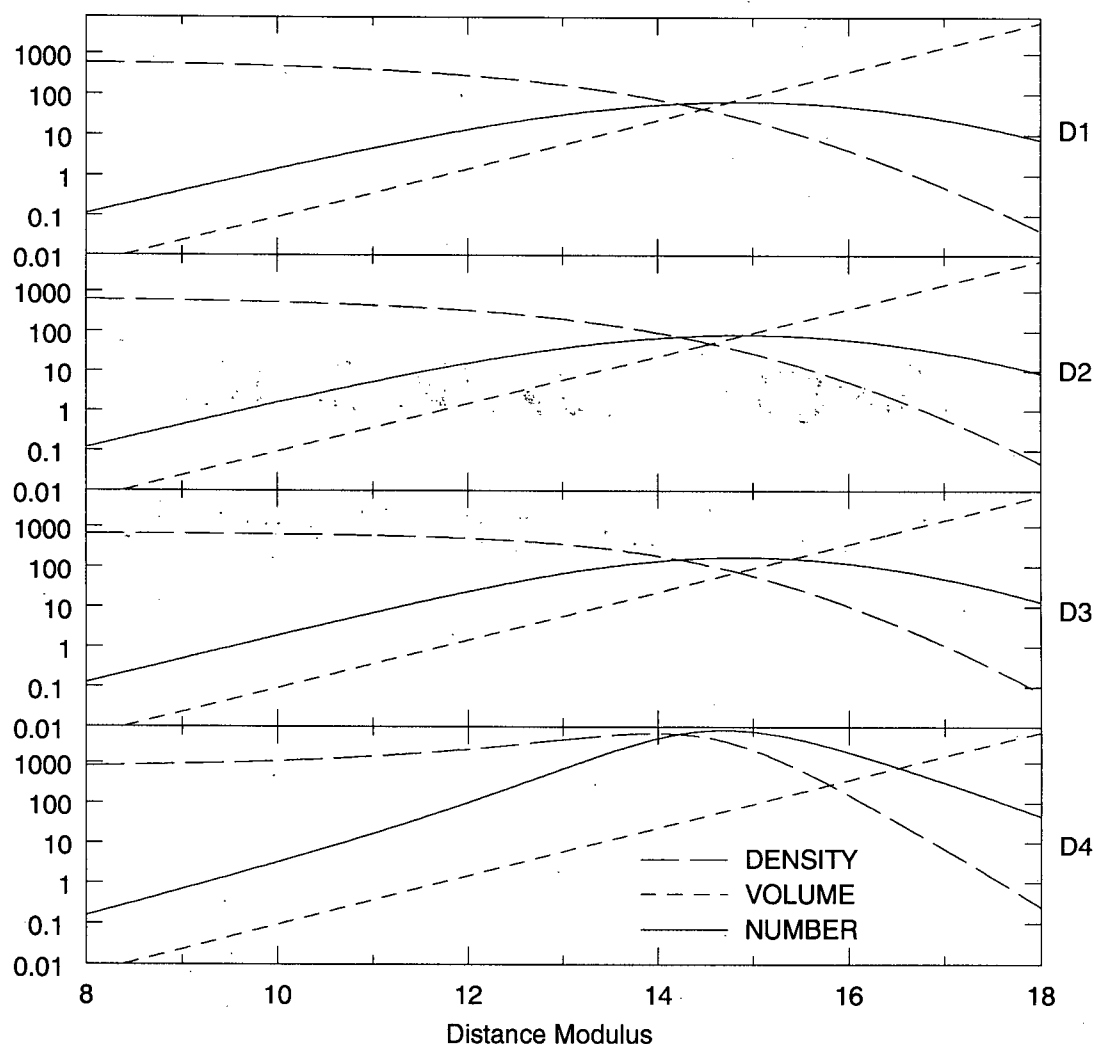


Figure 3.4: Relative number, relative number density, and relative volume as a function of distance modulus. These quantities are scaled so they will all fit in the same dynamic range, and hence the numbers do not have a physical meaning. The strong peak in the D4 field shows that the bulk of stars in this field are expected to be close to a distance modulus of 14.5. This results in the probability map for this field looking more like an isochrone than for the other fields.

Chapter 4

Data – Model comparison

4.1 Statistics

After the construction of a simulated data set, be it a Monte Carlo simulation or a probability map, the next step must be the comparison of the simulated data with the observed data. There were three methods that were used for this study, the χ^2 test, the Poisson likelihood ratio, and Bayesian inference. For all these methods it was necessary to bin the observed data into pixels. The pros and cons of each method will be discussed in the following sections which are based on an analysis performed by Dolphin (2002).

4.1.1 Gaussian Likelihood Ratio

Generally, when comparing a model with data the obvious choice of statistic to use is the χ^2 test. A χ^2 test measures the difference between a model and the data and, as such, is intuitive to understand, and comfortable to use. Indeed, this was the first method used for the analysis of our models. Furthermore, if the data has known uncertainties at each point and Gaussian error, minimizing χ^2 is a maximum-likelihood calculation. This is demonstrated in the following manner:

Let P denote the probability that the observation d is drawn from model m . P_i is the likelihood that a value of d_i is observed in bin i considering the model predicts a value of m_i in that pixel, and σ_i is the uncertainty of the bin. We can then write that

$$P_i = \sqrt{\frac{1}{2\pi\sigma_i^2}} e^{-0.5(d_i - m_i)^2 / \sigma_i^2} \quad (4.1)$$

We define a “Gaussian likelihood ratio”, GLR, as the probability that the observed data point d_i was drawn from a model equal to m_i divided by the probability that it was

drawn from a model equal to d_i .

$$GLR = \prod_i \sqrt{\frac{\sigma_{di}^2}{\sigma_{mi}^2}} e^{-0.5(d_i - m_i)^2 / \sigma_{mi}^2}. \quad (4.2)$$

By taking the logarithm of both sides, we obtain:

$$-2 \ln(GLR) = \sum_i \ln\left(\frac{\sigma_{mi}^2}{\sigma_{di}^2}\right) + \sum_i \frac{(d_i - m_i)^2}{\sigma_{mi}^2}, \quad (4.3)$$

or

$$-2 \ln(GLR) = \chi^2 + \sum_i \ln\left(\frac{\sigma_{mi}^2}{\sigma_{di}^2}\right). \quad (4.4)$$

If we can assume that the errors of the observations have a smooth Gaussian distribution and the σ_i values do not change during the fit then $\ln(\sigma_{mi}^2/\sigma_{ni}^2) = 0$ and minimizing χ^2 will determine the model most likely to have produced the observations. Unfortunately, neither of these conditions are true in the comparison in our situation. For the pixels to be small enough to resolve all the interesting features they will contain only a small number of stars. This means that we are dominated by Poisson errors rather than Gaussian errors. Second, $\ln(\sigma_{mi}^2/\sigma_{ni}^2)$ does not vanish. Mighell (1999) showed that the inappropriate use of χ^2 in a Poisson regime can lead to an incorrect value of the minimum (up to 42% in his example)[22].

4.1.2 Poisson Likelihood Ratio

The Poisson probability is defined as:

$$P_i = \frac{m_i^{d_i}}{e^{m_i} d_i!} \quad (4.5)$$

with m_i and d_i defined as in the previous section. When dealing with small numbers it is natural to define the ‘‘Poisson Likelihood Ratio’’, PLR . This is defined in a manner analogous to the definition Gaussian Likelihood Ratio. We obtain:

$$PLR = \prod_i \frac{m_i^{d_i} e^{d_i}}{d_i^{d_i} e^{d_i}} = \prod_i \left(\frac{m_i}{d_i}\right)^{d_i} e^{d_i - m_i}. \quad (4.6)$$

Analogously to the previous section, we can take the logarithm of the above expression and obtain the small number equivalent of χ^2 , namely

$$-2 \ln(PLR) = 2 \sum_i \left(m_i - d_i + d_i \ln \left(\frac{d_i}{m_i} \right) \right). \quad (4.7)$$

This statistic shares many features with the GLR, it vanishes for a particular pixel when model and data predict the same number, and has the same value of variance and expectation value for larger values of m_i .

4.1.3 Bayesian Inference

Both the above mentioned methods can compare observational data with both Monte Carlo simulations and probability maps. The “bin-free” method of Bayesian inference has the obvious advantage that it does not require the data to be binned, ensuring all the information in the data set is retained. However, this means that there is no natural way to use this statistic to compare observational data with a Monte Carlo simulation. Furthermore, to take full advantage of unbinned data one would have to construct a probability map such is a smoothly changing function of colour and magnitude. A method to do this remains unknown to me as of present.

Supposing one could construct a smoothly varying probability map, the probability of finding a star, j , at a certain position in colour-magnitude space is written as $P_j(c_j, m_j) / \sum_j m_j$, or just $P_j(c_j, m_j)$ assuming the sum of all probabilities over the entire colour-magnitude space is normalized to 1. Assuming that all the points are independent, the total probability is simply:

$$P = \prod_j P_j. \quad (4.8)$$

If the binning of colour-magnitude space is sufficiently fine (the bin size is much smaller than CMD features) then the probability will be close to constant over a bin. In this case, we can write the cumulative probability of all the points in a bin as

$$P_i = \left(\frac{m_i}{\sum_j m_j} \right)^{d_i}. \quad (4.9)$$

Thus, the total probability is

$$P = \prod_i \left(\frac{m_i}{\sum_j m_j} \right)^{d_i}. \quad (4.10)$$

As with *GLR* and *PLR* we now take the logarithm to obtain

$$-2 \ln(P) = \sum_i n_i \ln \left(\frac{m_i}{\sum_j m_j} \right). \quad (4.11)$$

If this binning is fine enough, equations 4.11 and 4.7 should find identical minima. For the purposes of this study, it was practical to bin quite finely. If one can use the *PLR*, the Bayesian inference method does not assist further to search for a minimum. It does not find a more secure value for a minimum, and is not normalized. However, it is useful as an indicator of the correct choice of pixel size. While we are not in danger of finding an erroneous minimum if the data is binned too finely, the signal to noise in a given pixel will decrease. Therefore, the error found on our solution will be greater if the binning is too fine. It is important to bin the data as coarsely as possible while still resolving all the features of the CMD, and obtaining the correct answer.

4.2 Parameter Search and Error Estimation

Efficiently searching a high-dimensional parameter space is a very challenging task. Over the course of this study three different methods were used. The first is the downhill simplex method, the second is the Monte Carlo Markov Chain and the third is the simple, but computationally expensive grid search. Each of these methods has its pros and cons. Each will be described in the following sections.

4.2.1 Searching Parameter Space

Downhill Simplex

The downhill simplex method was invented by Nelder and Mead in 1965. The appealing attribute of this method is that it only requires the ability to evaluate a function at a

particular location, and not the derivatives of the function. A simplex is a geometrical figure with $N + 1$ dimensions in an N -dimensional space. To be clear, in a 2-dimensional space, a simplex is a triangle.

For this project we used an algorithm described in Numerical Recipes called AMOEBA[24]. AMOEBA works by moving the simplex toward the minimum through a series of four possible types of steps. In the case of $N = 2$ a simplex is a triangle. Unfortunately, in multi-dimensional space it is impossible to bracket the minimum. One must initialize the simplex to some position. If the surface of the parameter space is smooth, the algorithm works regardless of the initial position of the simplex. However, if there are local minima the choice of the initial simplex can influence the minimum that AMOEBA will find.

The algorithm begins by evaluating the figure of merit of the fit (for this study PLR was used) at each vertex. The most basic move is the reflection of the highest point through the opposite side – in the $N = 2$ case the triangle flips over its downhill edge. The second type of move is related to the first. If AMOEBA can find a lower position by stretching in the direction of the vertex being moved it will do so – flip over the downhill edge and stretch. In this manner, AMOEBA can move quickly over flat smooth surfaces, and on steep descents. If everything works as it should, and indeed the function does minimize, eventually AMOEBA will approach a minimum. In this case, flipping the highest vertex over the downhill edge could move the vertex over the minimum, and back uphill. When AMOEBA finds itself in this situation there are two types of moves it may perform. Both involve shrinking the size of the simplex, allowing it to find a precise value for the minimum. AMOEBA may move the position of the highest vertex toward the downhill edge with no flip. Alternately, AMOEBA may move the highest two vertices toward the downhill vertex.

This is a very simple, but powerful algorithm. Unfortunately, our space was full of local minima. I postulate that these minima are not real, but are a product of the discreet nature of our dataset and of our simulated probability maps. Regardless of the nature of our local minima, they prevent the use of AMOEBA to search the global minimum.

Markov Chain Monte Carlo

The Markov Chain Monte Carlo (MCMC) is an interesting technique for finding a minimum in multi-dimensional parameter space. Like the downhill simplex method it does not require the calculation of derivatives of a function.

The core of the technique is very simple. Starting at a certain location \vec{x}_0 , one calculates the value of the fit (again PLR in our case), denoted $f(\vec{x}_0)$. Then a value for a location, \vec{x}_1 , randomly located within a n-dimensional box centered on \vec{x}_0 , $f(\vec{x}_1)$ is calculated. If the value of $\Delta f(\vec{x}_1)$ (defined as $f(\vec{x}_1) - f(\vec{x}_0)$) is negative, the process repeats starting now from \vec{x}_1 . If the value of $\Delta f(\vec{x}_1)$ is positive then the process repeats from \vec{x}_0 , and a new model is calculated from another random point replacing \vec{x}_1 . In this way the function will slowly be minimized. The collection of locations, $\vec{x}_0, \vec{x}_1, \dots, \vec{x}_n$ is in fact the Markov Chain. The process of getting reasonably close to the minimum is called the “burn-in” period. While each step during the burn-in can have any direction, the average of all the directions of the steps will be in some direction. Once the general area of the minimum is found, the algorithm continues as before. However, instead of progressing in a relatively straight line toward the minimum (as happens during the burn-in) the average direction of the steps will now be zero. Movement is guaranteed because the value of the “function” will not be the same for two realizations of the simulations with different random seeds. The simulation finishes after a certain number of iterations. The chain is then ‘pruned’ by removing the locations that are part of the burn-in. After the burn in, the number of steps at a given location will be proportional to the quality of fit at that point. Therefore, to estimate the value of the minimum one examines the distribution of the points. The beauty of the Markov Chain Monte Carlo is that the errors are determined in the course of finding a minimum. The distribution of points around the error gives the error estimate directly.

Simulated Annealing is a simple modification to the Markov Chain Monte Carlo designed to ensure that the entire parameter space is well sampled. This means that the starting point has little bearing on the subsequent behaviour of the Markov Chain.

To achieve this, the algorithm takes the counter-intuitive step of sometimes accepting a position \vec{x}_{n+1} even if $f(\vec{x}_{n+1})$ is greater than $f(\vec{x}_n)$. This means that the chain can cross between widely separated peaks of probability. This is achieved by giving the algorithm a “temperature”, T . The probability of the chain accepting a point with a poorer fit is proportional to $e^{-\Delta f(\vec{x}_n)/T}$. The temperature is high during the initial stages of the simulation. This ensures that the the location of \vec{x}_n will move relatively quickly away from the point of initialization, and will sample a good fraction of parameter space. As the simulation continues, T decreases slowly, eventually making it virtually impossible for the Markov Chain to accept steps that involve a positive $\Delta f(\vec{x}_n)$.

The number of projects that use MCMCs is growing steadily, but the process remains a ‘black art’, i.e. a rigorous prescription of how to apply the MCMC to a particular problem does not exist. The choice of initial temperature, cooling rate, the size of the box in which to search for a new point, the length of the burn-in, and the number of iterations to include in the simulation are left to the designer of each particular MCMC. Very vague guidelines, such as the MCMC should accept approximately 50% of steps during the burn-in, can be found scattered throughout the literature, but a definitive guide does not exist.

Grid Search

The simplest type of search for a minimum in parameter space is just to search the entire parameter space. If the defined boundaries bracket the minimum, then one is guaranteed to find the global minimum. The drawback of the grid search is that it is extremely computational expensive. This problem is particularly pronounced if one is trying to find a minimum in a high-dimensional space. Efficiency is maximized with a judicious choice of search boundaries and spacing.

For this thesis, we never searched in a space of dimension higher than four. Furthermore, the values of the parameters we were searching were all confined to a relatively small range. We found a grid search to be acceptable for these purposes. All results shown in this thesis were obtained using a grid search.

However, when this project is extended to include the thick and thin disks, this search technique will cease to be a viable method for finding the minimum.

4.2.2 Error Estimation

One attractive aspect of the Markov Chain Monte Carlo is the fact that error estimation is an integral part of the parameter estimation. For both the grid search and the downhill simplex method, uncertainties are not obtained so naturally. For our purposes the Bootstrap method was the simplest method of estimating our uncertainties. The bootstrap method, invented by Efron in 1979, allows one to obtain many ‘sample’ datasets from a single observed data set. It seems like one is getting something for nothing. The method is named after the image of achieving goals with no external help – pulling oneself up by one’s bootstraps.

This method creates a simulated dataset by randomly sampling the observed data with replacement. Each star is labeled. N random numbers are drawn from a range of 1 to N , where N is the number of stars in the original dataset. For each random number drawn, the corresponding star is copied to a list. In this manner a new dataset is composed of the same length of the original observed dataset. The fit is then calculate with the new data set. In this way one can obtain a distribution of values of the fit, and hence an estimate of the errors.

Chapter 5

Constraints on Parameters

At the time of writing, the model definition remains incomplete. The derived error on the best estimates of our parameters are larger than we expect. All results stated here are preliminary.

The goal of this project was to constrain the value of the four parameters necessary to describe completely the Galactic halo. The constraints put on the parameters will be discussed in the following section. The dependence of two parameters at a time on contour plots will be shown. Note that in all the plots the contours are exponentially spaced. The one-sigma errors, determined from bootstrapped datasets, are shown as dashed lines. These errors were determined at the best-fitting model, and were assumed to be somewhat insensitive to small displacements in parameter space. We were most interested in determining the initial-mass function and half-light radius. The plots 5.1, 5.2, 5.3, and 5.4 show how the fit varies with initial-mass function and half-light radius for the four fields, D1, D2, D3, and D4. Following the aforementioned plots, all subsequent plots will be for the ‘representative’ field D1 unless otherwise stated. D1 was chosen because, like D2, it has a monotonically decreasing stellar density along the line of sight. Both D3 and D4 peak at some point, making the true determination of the fit, especially half-light radius, problematic.

5.1 Initial Mass Function

One of the most important parameters to understand when studying stellar populations is the number of stars of various masses of a freshly formed population. This quantity is called the initial mass function, $\xi(M)$. Specifically, the number of stars of a mass

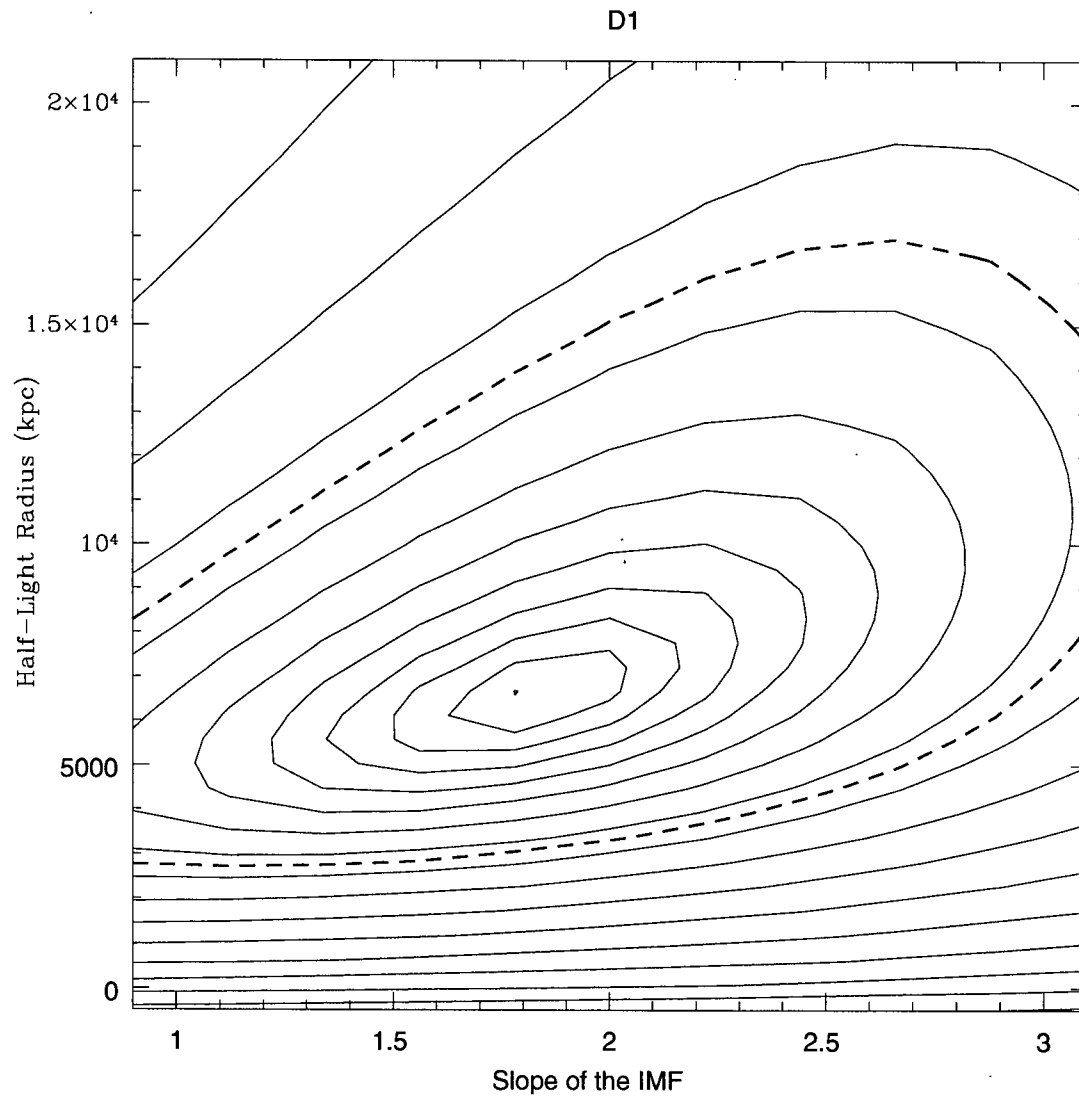


Figure 5.1: Contours showing the goodness of fit varying with IMF and HLR for the field D1. Binary fraction is fixed to 35% and axial ratio is set to 1.

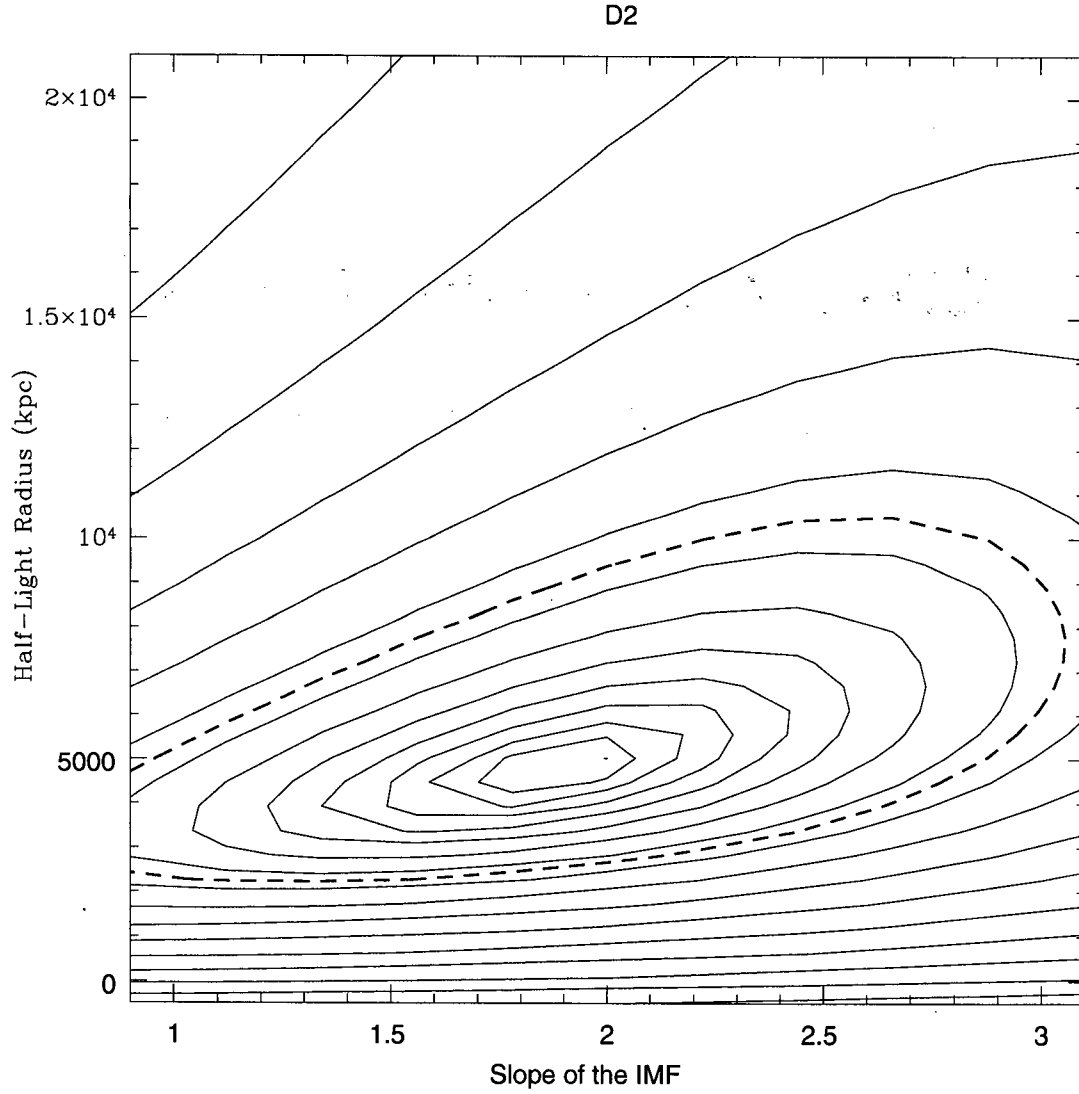


Figure 5.2: Contours showing the goodness of fit varying with IMF and HLR for the field D2. Binary fraction is fixed to 35% and axial ratio is set to 1.

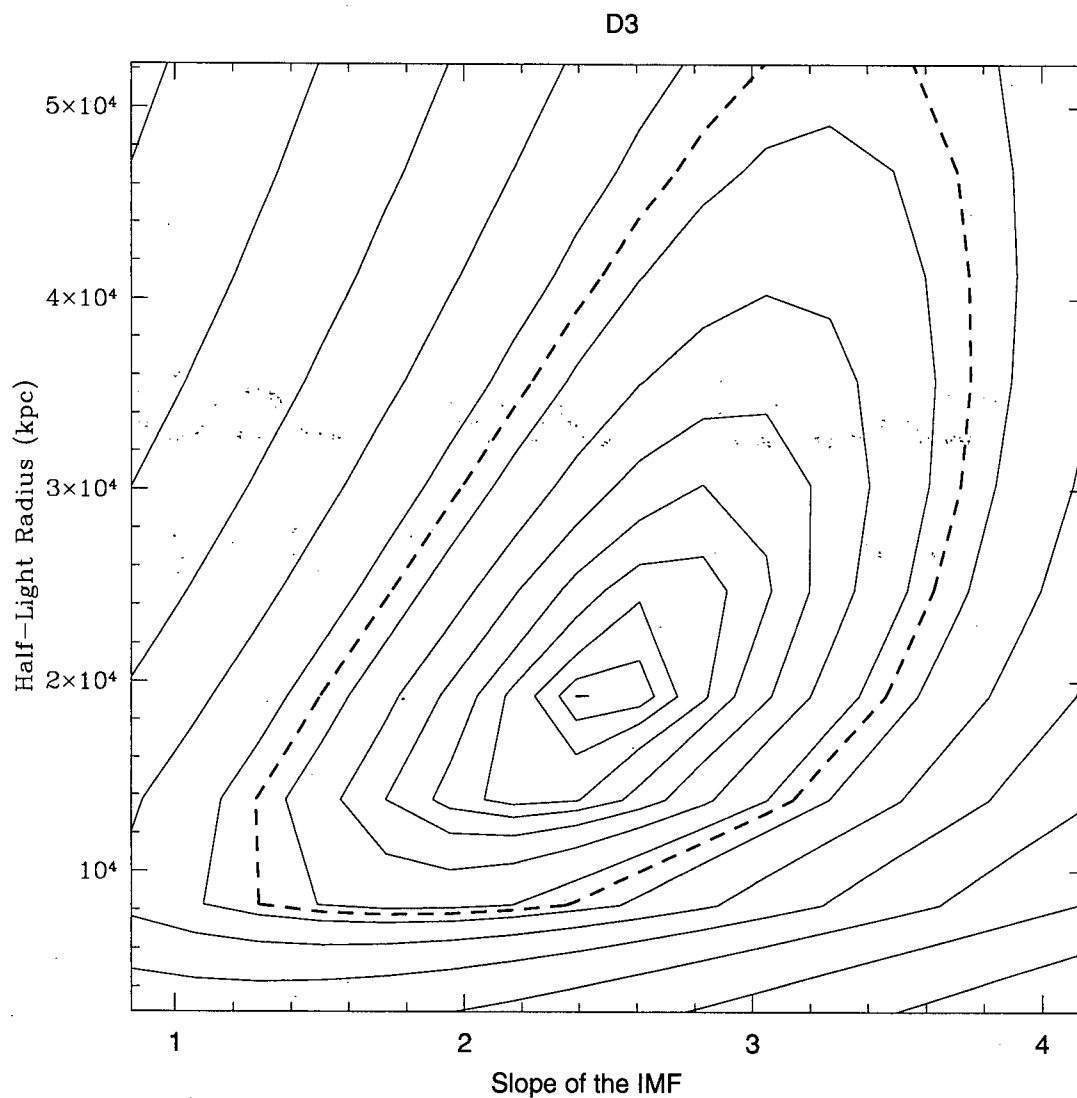


Figure 5.3: Contours showing the goodness of fit varying with IMF and HLR for the field D3. Binary fraction is fixed to 35% and axial ratio is set to 1. Note the unphysically high value of the half-light radius. It is postulated that this is due to the fact that the density profile along this line of sight is not monotonically decreasing, but rather has a peak.

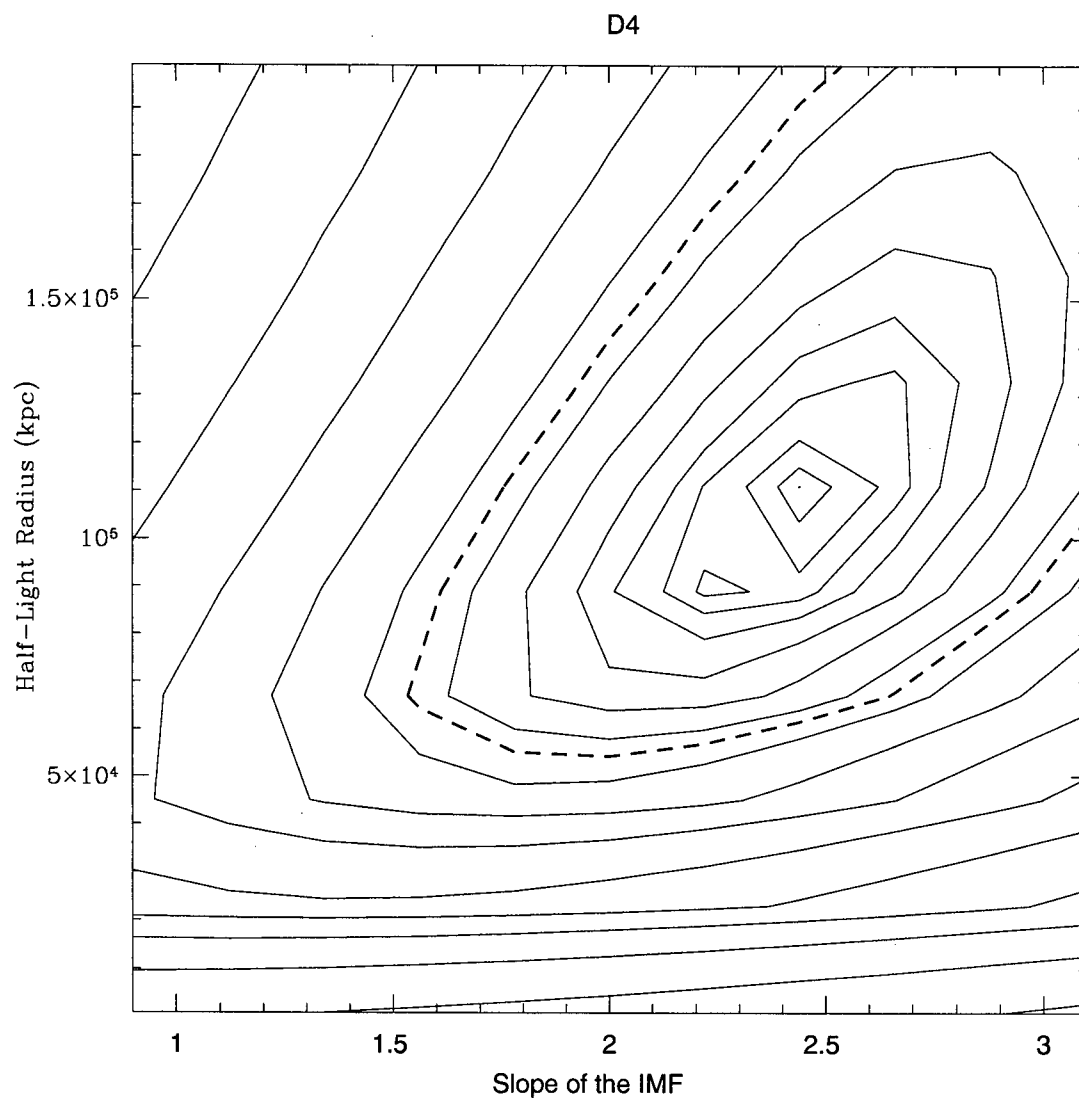


Figure 5.4: Contours showing the goodness of fit varying with IMF and HLR for the field D4. Binary fraction is fixed to 35% and axial ratio is set to 1. Note the unphysically high value of the half-light radius. It is postulated that this is due to the fact that the density profile along this line of sight is not monotonically decreasing, but rather has a peak.

between M and $M + dM$ can be written in the form:

$$dN = N_0 \xi(M) dM \quad (5.1)$$

where N_0 is some normalizing constant. If we require that

$$\int_M N_0 \xi(M) dM = 1 M_\odot \quad (5.2)$$

then N_0 represents the number of solar mass stars in a freshly formed population of stars. This is a difficult quantity to determine directly for a general population of stars. If a population of stars is coeval, as in a cluster, one can measure a related quantity, the luminosity function, allowing the derivation of the IMF. In 1955 Salpeter [30] postulated that the IMF could be well represented by a power law of the form

$$\xi \propto M^{-\alpha}. \quad (5.3)$$

Salpeter found that

$$\xi \propto M^{-2.35}. \quad (5.4)$$

This form of the IMF is known as the Salpeter IMF. While equation 5.3 may be valid for a large range of masses, it can not be true for all masses. This is because if $\alpha < 2$ the total mass involved in a starburst diverges at high masses, while if $\alpha > 2$ total mass diverges for low masses. This implies that α changes as a function of mass.

In 1986 Scalo published a study advocating an IMF described by a three part broken power law with $\alpha < 2$ at low mass and $\alpha > 2$ at high masses [31]. A broken power law is generally accepted now, but the location of the breaks, and the slopes of the individual sections remains somewhat indeterminate. The effects of metallicity on IMF are poorly understood. Theory suggests that without metals to aid in the cooling process, much larger masses of gas will fragment out of giant molecular clouds. This would imply a flatter slope at the high end of the IMF for low metallicity populations.

In this thesis we attempt to constrain the slope of the IMF of stars from a mass of $\sim 0.4 M_\odot$ to the halo turn off ($\sim 0.8 M_\odot$). We found the initial-mass function to be slightly flatter than Salpeter, i.e. $\alpha < 2.35$. The plots 5.5 and 5.6 show the dependence of the fit on the slope of the IMF on binary fraction and axial ratio respectively.

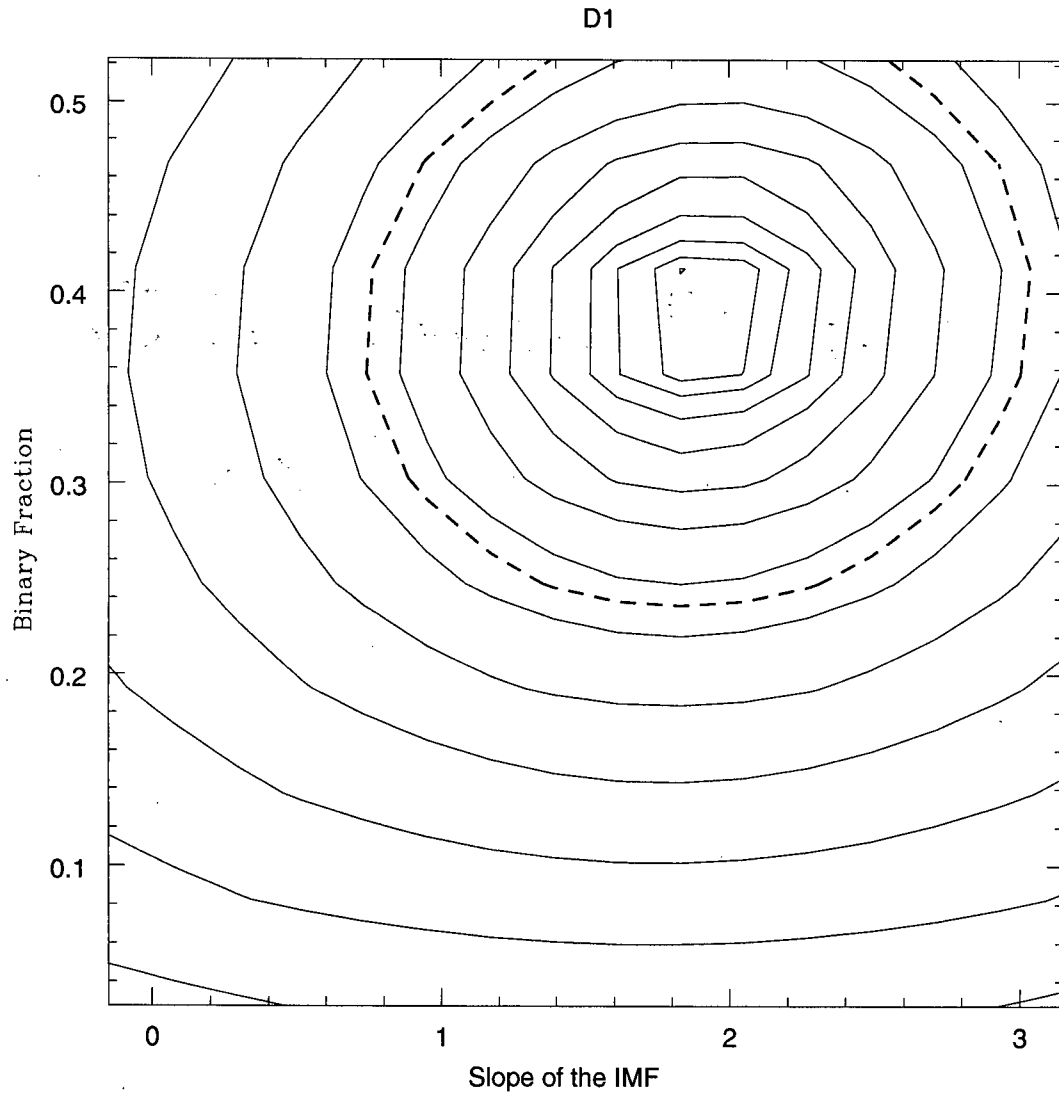


Figure 5.5: Contours showing the goodness of fit varying with IMF and binary fraction. Half-light radius is fixed to 7 *kpc* and axial ratio is set to 1.

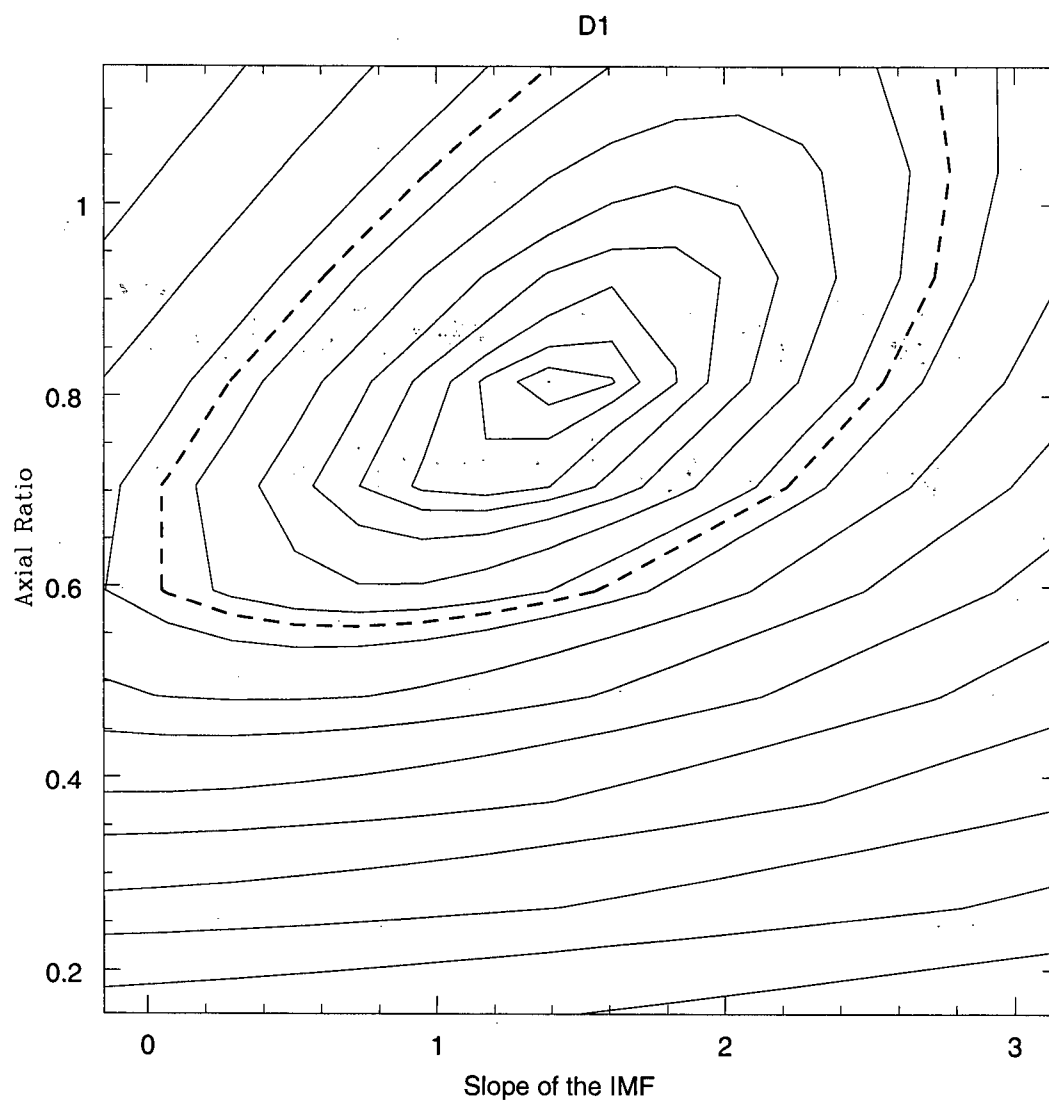


Figure 5.6: Contours showing the goodness of fit varying with IMF and axial ratio. Half-light radius is fixed to 7 *kpc* and binary fraction is set to 0.35.

5.2 Physical size

The stellar halo of the Milky Way is an important, but poorly studied, component of our Galaxy. Fundamental to our understanding of the halo is knowledge of its physical dimension. The form of the density profile of the Galaxy is uncertain. It is typically modeled as a de-projected de Vaucouleurs profile or a power law. If the halo density profile is a de Vaucouleurs profile, the physical size of the halo is described by a characteristic radius, R_0 . If the density profile is a power law, the physical size is measured by the power-law index, and a characteristic scale. For this study we used a de-projected de Vaucouleurs profile. The density as a function of Galactocentric distance, $\rho(R)$ is written as

$$\rho(R) = \exp \left(\frac{-7.6 \left(\frac{R}{R_0} \right)^{\frac{1}{4}}}{\left(\frac{R}{R_0} \right)^{\frac{3}{4}}} \right) \sqrt{0.05 \left(\frac{R_0}{R} \right)^{\frac{1}{4}}} \quad (5.5)$$

where R_0 is the half-light radius of the Galaxy.

The best values for half-light radii were found to be higher than Bahcall's estimate [1]. Furthermore, there is a degeneracy between half-light radius and axial ratio. In fact, for the D3 and D4 fields, extremely large values of half-light radius coupled with a small value of axial ratio are favoured over half-light values more in accordance with the literature value [1]. The dependence of the fit on half-light radius and binary fraction (fraction of stars found in binary systems) and axial ratio are shown in figures 5.7 and 5.8.

5.3 Axial ratio

Halo stars formed when the ISM was very metal poor – before star formation in the Galaxy, and subsequent evolution, had time to enrich the ISM. This means that they formed when the Galaxy was very young, and therefore contain information about the environment in which the Milky Way formed. One of the most interesting unknowns is the dynamical environment from which the Galaxy was formed. The axial ratio gives

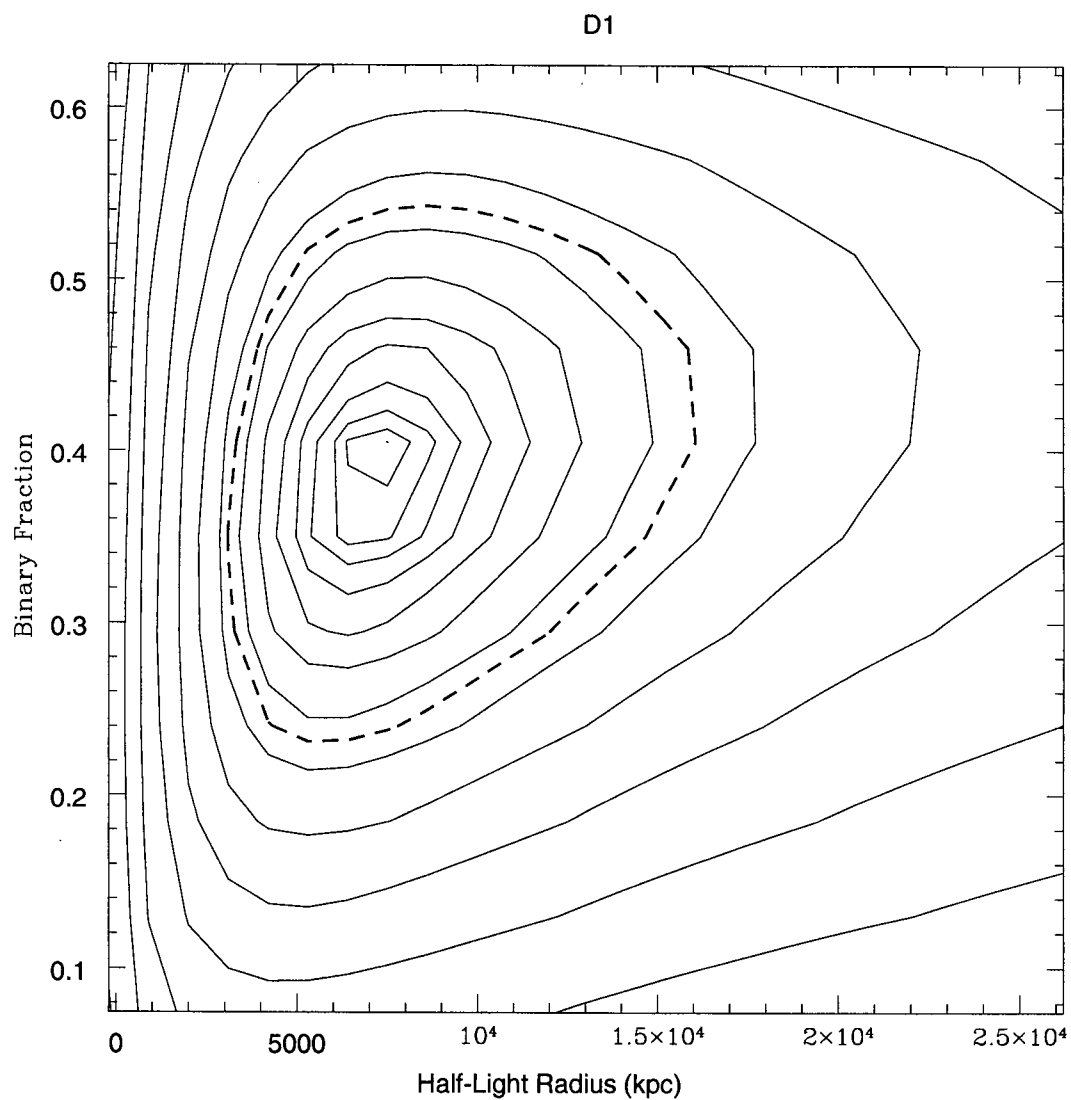


Figure 5.7: Contours showing the goodness of fit varying with binary fraction and HLR. Slope of the IMF is held at 2, and binary fraction is set to 35%.

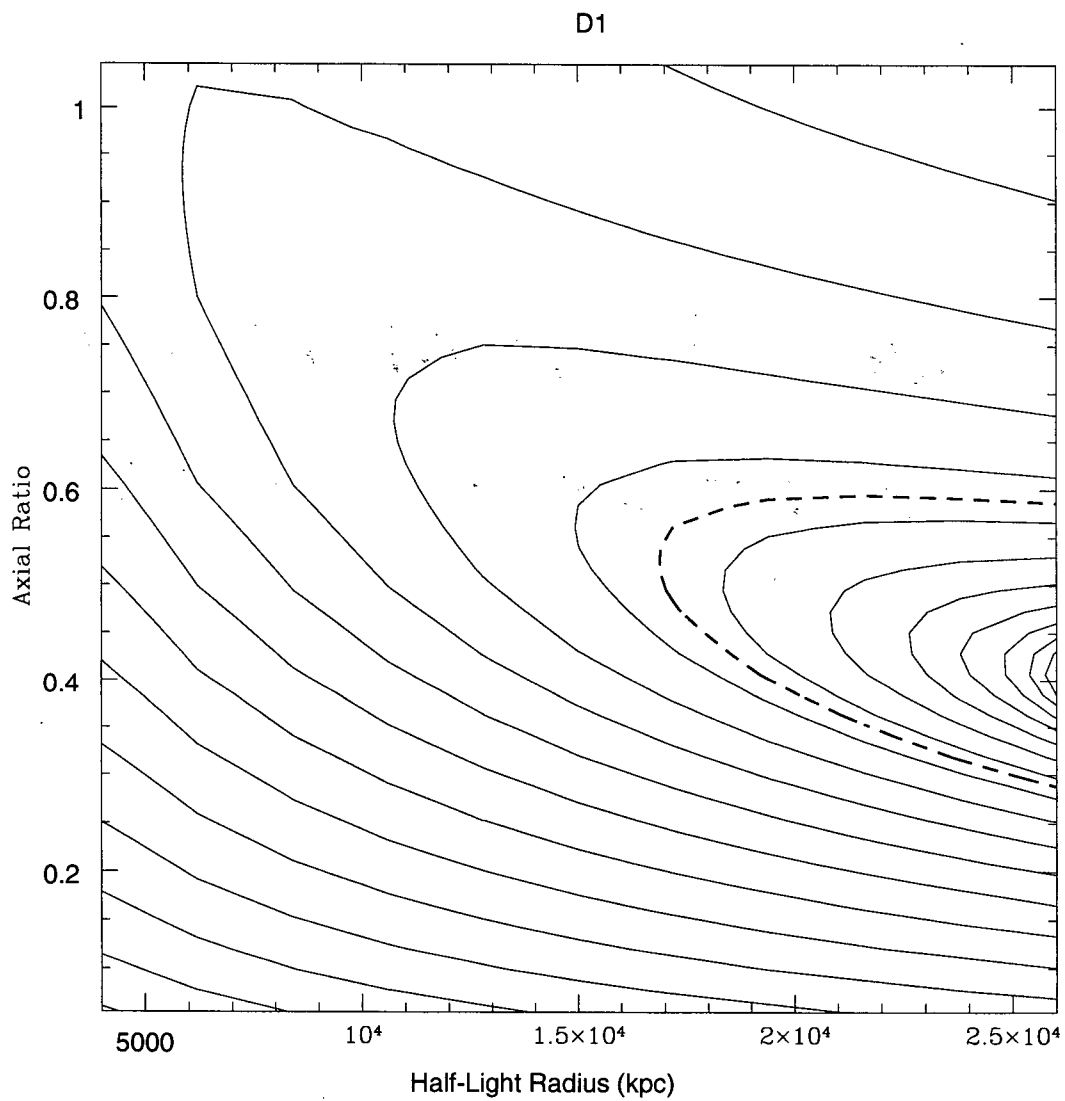


Figure 5.8: Contours showing the goodness of fit varying with HLR and axial ratio. Slope of IMF is fixed to 2 and binary fraction is set to 35%.

information on this. The flattening of the halo is described by the ratio of its major to minor axes – c/a . The literature values have quite a range for this parameter, from as high as 1 [28] to as low as 0.5 [6]. This parameter has interesting implications for theories seeking to explain the origin and dynamics of the halo[4]. For instance, numerical simulations of Λ -CDM galaxy formation predict that dark matter halos should have axial ratios between 0.6 – 0.8 [12]. If there is coupling between the dark matter halo and the stellar halo, or if they have a common dynamical origin, one would expect the stellar halo to be flattened in a similar manner[28].

For our best estimates of half-light radius, the axial ratio minimized to ~ 0.9 . The number of stars at a particular distance is a product of the half-light radius and the axial ratio. Because of this, for any one direction there is a degeneracy between axial ratio and half-light radius. This is shown in figure 5.8. We had hoped that we would be able to break the degeneracy by combining information from fields in different directions. This possibility is still being investigated.

5.4 Binary fraction

Because the solar neighbourhood is dominated by stars from the thin disk, one can discover the binary fraction for this component relatively easily. The disk binary fraction is approximately 50%[5]. The paucity of halo stars in the solar neighbourhood makes the binary fraction of the halo much harder to determine. Most constraints come from spectroscopic studies of high-velocity stars. The results of these studies are somewhat inconclusive. Some suggest that the binary fraction is independent of metallicity [18], while other studies favour a smaller binary fraction for halo stars ($\sim 20\%$)[29]. A recently published study of Messier 4 that I was involved in found that the observed CMD was best fit by a binary fraction of several percent[27]. The significance of the M4 result is unclear as the binary fraction is subject to dynamical effects. It is important to determine the halo binary fraction for star-count studies because it is degenerate with the half-light radius. Many models assume of 50% binary fraction. In 2002, Siegel[36] showed that this

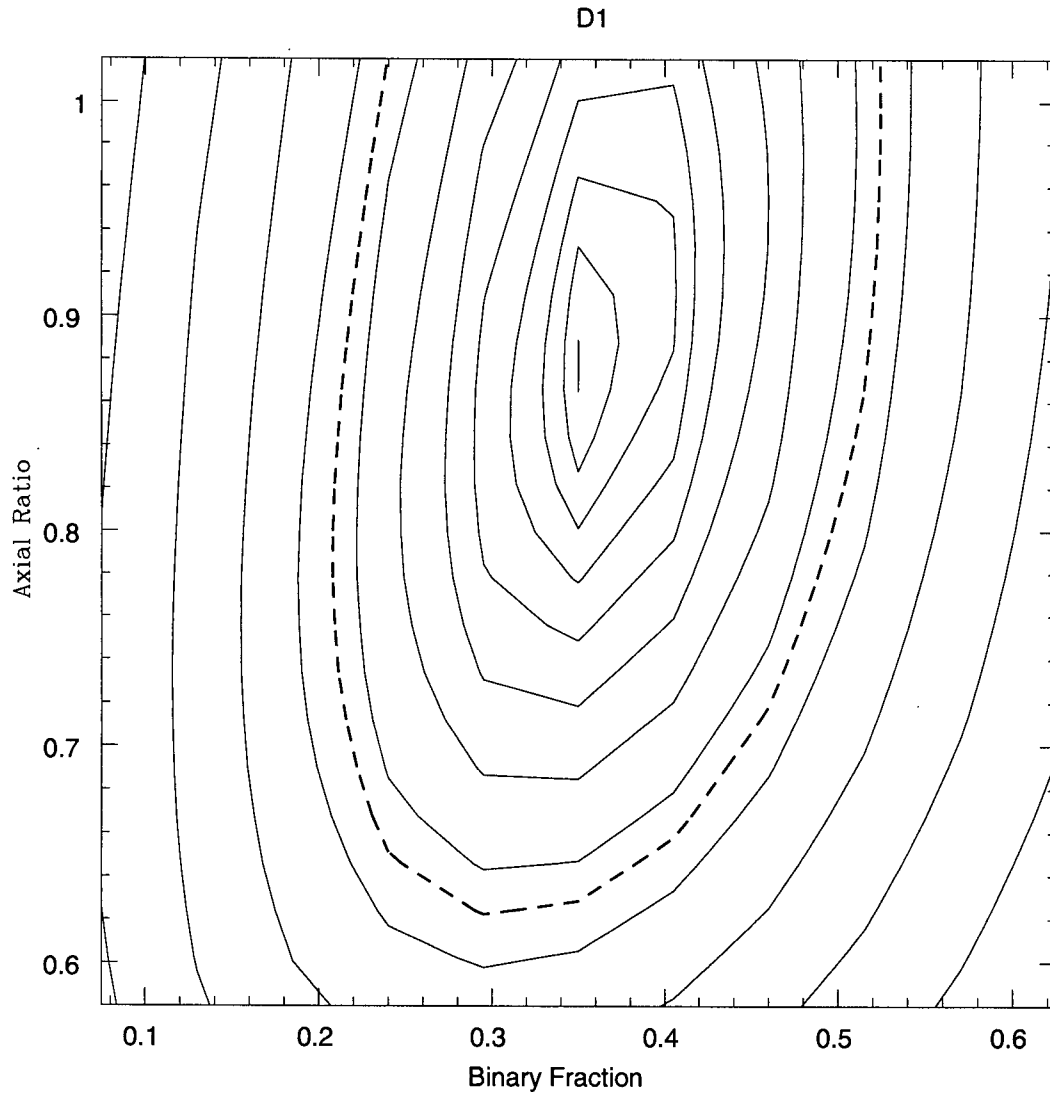


Figure 5.9: Contours showing the goodness of fit varying with binary fraction and axial ratio. Half-light radius is fixed to 7 kpc and slope of the IMF is set to 2.

assumption can lead to significant ($\sim 20\%$) errors on derived scale lengths and heights.

The binary fraction was the most tightly constrained parameter in our study. It minimized to a physically reasonable value for almost every other combination of parameters. The value was typically $\sim 35\%$, with the one sigma error bars constraining the value between $20\% - 50\%$. The dependence of the fit on binary fraction and axial ratio is shown in figure 5.9.

Chapter 6

Conclusions and Discussion

6.1 Conclusions

This project has developed a framework within which to conduct star-count studies, and has set the stage for a more in depth study. Some of the key findings related to the development of the project are listed below.

- This study suggests, that because of the difficulty in distinguishing stars from galaxies at very faint magnitudes, the practical limit to depth for a ground based star-counting study may be close to $g = 25$ no matter how much telescope time one can get.
- Monte Carlo simulations are a working method with which to conduct star-count studies. However, they are computationally expensive, and are therefore only viable if one has extensive computational resources.
- Because of its low computational expense, probability mapping is the preferred method with which to conduct star-count studies. However, it is impossible to determine the local density of halo stars via this method. Monte Carlo simulations remain the only way to determine the local density of halo stars.
- If colour – magnitude space is correctly binned, minimizing Poisson Likelihood Ratio (PLR) and maximizing probability via Bayesian inference will lead to the same conclusions. This means that we have an independent measure with which to determine the correct bin size.

- Markov Chain Monte Carlo simulations, downhill simplex methods, and grid searches are all valid methods with which to determine a maximum likelihood. However, MCMC simulations are computationally expensive, and downhill simplex methods are sensitive to local maxima. For a low dimensional ($N \sim 5$) the grid search is not too computationally expensive, and gives a sense of the overall shape of the fitting surface. It was the preferred choice for studying the halo. However, for studies of the disk, this method would be prohibitively slow.

6.2 Discussion

The principle of analyzing only one component of the Galaxy at a time is good in theory, but has some practical difficulties. There are two obvious, and related, points. First, one has to worry about contamination from the components not being modeled. The results obtained were somewhat sensitive to our (arbitrary) choice of where the thick disk contamination was ‘low enough’. Because we cannot identify the population that a particular star is drawn from, a quantitative choice is difficult to make. We simply had to examine colour-magnitude diagrams by eye, and estimate. Second, in order to examine the halo exclusively, severe restrictions in colour-magnitude space must be implemented. This in turn restricts the physical range of stars that may be studied. For our choice of colour cut, we were limited to stars more massive than $0.4M_{\odot}$. As the range of masses examined shrinks, the range of the slope of the IMF, and all its associated degeneracies, that can acceptably reproduce the observations grows.

6.3 Future Work

There is a vast amount of fascinating work to be performed in this field. The CFHTLS represents a truly unique dataset for this type of project.

The penultimate stage of this project will focus on fields that are comprised primarily of thick disk and halo stars in a large section of colour-magnitude space. Fields with

moderate Galactic latitudes are ideal for this purpose. There are several of these fields in the Canada-France-Hawaii Telescope Open Star Cluster Survey (CFHT-OSCS) such as the background of NGC6819. Furthermore, the CFHTLS-Wide survey will yield the depth and area necessary to put tight constraints of the parameters describing the thick disk.

Finally, detailed studies of the thin disk will be performed. For this section of the study, the data from the CFHT-OSCS will be indispensable. The fact that these fields contain stellar clusters allows us to get an accurate idea of the dust distribution between the Sun and the cluster. This study has years of work left in it, and each section promises to yield fascinating results.

Bibliography

- [1] Bahcall, J. N. & Soneira, R. M. 1980, ApJ, 238, L17
- [2] Basinski, J. M., Bok, B. J., & Bok, P. F. 1967, MNRAS, 137, 55
- [3] Bertin, E. & Arnouts, S. 1996, A&AS, 117, 393
- [4] Binney, James; Merrifield, Michael (1998), Galactic Astronomy, Princeton, Princeton University Press.
- [5] Carroll, Bradley; Ostlie, Dale; (1996) An Introduction to Astrophysics, New York, Addison-Wesley Publishing Company, Inc.
- [6] Chen, B., et al. 2001, ApJ, 553, 184
- [7] Dolphin, A. E. 2002, MNRAS, 332, 91
- [8] Fan, X. 1999, AJ, 117, 2528
- [9] Goldberg, L. 1939, Science, 90, 110
- [10] Harmon, R. & Mamon, G. 1993, ASP Conf. Ser. 43: Sky Surveys. Protostars to Protogalaxies, 15
- [11] Harris, W. E., Fitzgerald, M. P., & Reed, B. C. 1981, PASP, 93, 507
- [12] Helmi, A. 2004, Publications of the Astronomical Society of Australia, 21, 212
- [13] Jones, L. R., Fong, R., Shanks, T., Ellis, R. S., & Peterson, B. A. 1991, MNRAS, 249, 481

- [14] Kron, R. G. 1980, *ApJS*, 43, 305
- [15] Landolt, A. U. 1983, *AJ*, 88, 439
- [16] Landolt, A. U. 1992, *AJ*, 104, 340
- [17] Landolt, A. U. 1995, *VizieR Online Data Catalog*, 2118, 0
- [18] Latham, D. W., Stefanik, R. P., Torres, G., Davis, R. J., Mazeh, T., Carney, B. W., Laird, J. B., & Morse, J. A. 2002, *AJ*, 124, 1144
- [19] Le Fevre, O., Bijaoui, A., Mathez, G., Picat, J. P., & Lelievre, G. 1986, *aap*, 154, 92
- [20] Maddox, S. J., Efstathiou, G., & Sutherland, W. J. 1990, *MNRAS*, 246, 433
- [21] Lemon, D. J., Wyse, R. F. G., Liske, J., Driver, S. P., & Horne, K. 2004, *MNRAS*, 347, 1043
- [22] Mighell, K. J. 1999, *ApJ*, 518, 380
- [23] Oort, J. H. 1928, *bain*, 4, 269
- [24] Press, W. H., Teukolsky, S. A., Vetterling, W. T., & Flannery, B. P. 1992, Cambridge: University Press, —c1992, 2nd ed.
- [25] Reid, N. & Gilmore, G. 1982, *MNRAS*, 201, 73
- [26] Reid, I. N., Yan, L., Majewski, S., Thompson, I., & Smail, I. 1996, *AJ*, 112, 1472
- [27] Richer, H. B., et al. 2004, *AJ*, 127, 2771
- [28] Robin, A. C., Reyl  , C., & Cr  z  , M. 2000, *AAP*, 359, 103
- [29] Ryan, S. G. 1992, *AJ*, 104, 1144
- [30] Salpeter, E. E. 1955, *ApJ*, 121, 161
- [31] Scalo, J. M. 1986, *Fundamentals of Cosmic Physics*, 11, 1

- [32] Seares, F. H. 1931, PASP, 43, 371
- [33] Seares, F. H. & van Rhijn, P. J. 1925, Proceedings of the National Academy of Science, 11, 358
- [34] Sebok, W. L. 1979, AJ, 84, 1526
- [35] Schlegel, D. J., Finkbeiner, D. P., & Davis, M. 1998, ApJ, 500, 525
- [36] Siegel, M. H., Majewski, S. R., Reid, I. N., & Thompson, I. B. 2002, ApJ, 578, 151
- [37] Vallenari, A., Bertelli, G., & Schmidtobreick, L. 2000, AAP, 364, 925